

# Identification of Physiological Response Functions to Correct for Fluctuations in Resting-State fMRI related to Heart Rate and Respiration

Michalis Kassinos<sup>1</sup>, Georgios D. Mitsis<sup>2</sup>

<sup>1</sup>Graduate Program in Biological and Biomedical Engineering, McGill University, Montreal, QC, Canada

<sup>2</sup>Department of Bioengineering, McGill University, Montreal, QC, Canada

## **Abstract**

Functional magnetic resonance imaging (fMRI) is widely viewed as the gold standard for studying brain function due to its high spatial resolution and non-invasive nature. However, it is well established that changes in breathing patterns and heart rate strongly influence the blood oxygen-level dependent (BOLD) fMRI signal and this, in turn, can have considerable effects on fMRI studies, particularly resting-state studies. The dynamic effects of physiological processes are often quantified by using convolution models along with simultaneously recorded physiological data. In this context, physiological response function (*PRF*) curves (cardiac and respiratory response functions), which are convolved with the corresponding physiological fluctuations, are commonly employed. Initially, these *PRF* curves were assumed to be identical across subjects, but more recently, the use of subject-specific *PRF* curves has been suggested (derived by e.g. using the global fMRI signal). In the present study, we propose a novel framework for the robust estimation of *PRF* curves and use this framework to rigorously examine the implications of using population-, subject-, session- and scan-specific *PRF* curves. The proposed framework was tested on resting-state fMRI and physiological data from the Human Connectome Project. Our results suggest that *PRF* curves vary significantly across subjects and, to a lesser extent, across sessions from the same subject. These differences can be partly attributed to physiological variables such as the mean and variance of the heart rate during the scan. The proposed methodological framework can be used to obtain robust scan-specific *PRF* curves from data records with duration longer than 5 minutes, exhibiting significantly improved performance compared to previously defined canonical cardiac and respiration response functions. Besides removing physiological confounds from the BOLD signal, accurate modeling of subject- (or session-/scan-) specific *PRF* curves is of importance in studies that involve populations with altered vascular responses, such as aging subjects.

## 1. Introduction

Over the last few decades, advances in neuroimaging methods have significantly facilitated the study of brain function. One of the most popular methods for measuring brain activity is functional magnetic resonance imaging (fMRI), due to its high spatial resolution and non-invasive nature. fMRI, in principle, allows the mapping of brain function by measuring the hemodynamic response that accompanies neuronal activity in the brain. The onset of neuronal activity leads to physiological changes in the cerebrovascular system, including changes in cerebral blood flow (CBF), cerebral blood volume (CBV) per unit of brain tissue, as well as oxyhemoglobin and deoxyhemoglobin concentrations. The majority of fMRI studies is based on the blood oxygen-level dependent (BOLD) contrast mechanism, which primarily corresponds to the concentration of deoxyhemoglobin, and, thus, reflects a complex interplay of the aforementioned physiological processes (Ogawa and Lee, 1990).

Intriguingly, low-frequency ( $< 0.15$  Hz) fluctuations of the BOLD fMRI signal in the resting brain have consistently revealed significant correlations between distinct brain regions giving rise to a number of functional networks, termed resting-state networks (RSNs) (Biswal et al., 1995; Smith et al., 2009). Furthermore, several studies have reported alterations of RSNs in a range of cerebrovascular and mental disorders, demonstrating their potential use as biomarkers (Demirtaş et al., 2016; Leonardi et al., 2013; Sheline et al., 2010; Woodward and Cascio, 2015). Therefore, while fMRI studies were initially focused on studying the function of individual brain regions in response to specific tasks, during the last two decades or so there has been a shift towards understanding the correlation between distinct brain regions during rest, referred to as resting-state functional connectivity (rs-FC; van den Heuvel and Hulshoff Pol, 2010).

However, the interpretation of rs-FC studies is often questioned, partly because of the challenge of disentangling the neuronal component of the BOLD signal, which is typically of interest, from measurement and physiological confounds (Bright and Murphy, 2015; Murphy et al., 2009). These confounds may be related to scanner hardware drifts and instabilities, head motion as well as spontaneous physiological fluctuations, including respiration, cardiac activity and arterial CO<sub>2</sub> (Caballero-Gaudes and Reynolds, 2017; Liang et al., 2015; Murphy et al., 2013; Wise et al., 2004). For instance, fluctuations in the BOLD signal arise from cardiac pulsation, which pushes the brainstem into the surrounding brain tissue, causing deformation and cerebrospinal fluid movement (Dagli et al., 1999) while respiration-induced fluctuations result partly from respiration-related bulk movement of the head (Hu et al., 1995). Also, variations in the rate or depth of respiration have an impact on the arterial tension of CO<sub>2</sub>, which is a potent vasodilator and can therefore induce changes in CBF (Birn et al., 2006; Wise et al., 2004). In turn, global CBF changes cause low-frequency ( $\sim 0.1$  Hz) fluctuations in the BOLD signal, which may be misinterpreted as neuronal activity (Birn et al., 2006, 2008). In addition, it has been shown that fluctuations in the BOLD signal are caused by spontaneous fluctuations in heart rate (Napadow et al., 2008; Shmueli et al., 2007). These physiological-related fluctuations can have considerable impact on the resulting rs-FC patterns, including dynamic rs-FC patterns, as they tend to inflate the correlation between areas affected by physiological noise (Birn et al., 2008; Nikolaou et al., 2016). Therefore, several physiological noise correction techniques have been developed to remove the effects of physiological factors from fMRI data.

One of the most widely used methods for fMRI physiological noise correction is RETROICOR, proposed by Glover et al. (2000). According to this method, the pulsatility of blood flow and respiration-related motion are considered to distort the BOLD signal inducing an artifact that is time-locked to the cardiac and respiratory phases. Therefore, the associated physiological regressors are estimated as a linear combination of sinusoidal signals coinciding with the cardiac and respiratory cycles using concurrent cardiac and respiratory measurements and subsequently regressed out. RETROICOR can effectively remove the high-frequency cardiac ( $\sim 1$  Hz) and respiratory ( $\sim 0.3$  Hz) artifacts, despite the aliasing that takes place in a typical fMRI acquisition with a relatively low sampling rate (e.g. TR=3 s; Jones et al., 2008).

Cardiac and respiratory recordings can be also used for reducing low-frequency BOLD fluctuations associated with changes in heart rate and breathing patterns using physiological response function (PRF) models, such as the ones proposed by Chang et al. (2009) and Birn et al. (2006, 2008). In the first model, heart rate (HR) values, extracted from cardiac measurements, are convolved with the so-called cardiac response function (CRF). According to the second model, respiration volume per time (RVT), which is a measure proportional to the breathing rate (BR) and depth at each

time point, is initially estimated based on measurements from a pneumatic belt. Subsequently, RVT is convolved with the respiration response function (*RRF*) to estimate BOLD fluctuations due to changes in the breathing pattern. Both models are implemented in major fMRI preprocessing toolboxes such as the physiological noise modelling (PNM) toolbox of FSL (Jenkinson et al., 2012) and the PhysIO SPM toolbox (Kasper et al., 2017). Nevertheless, their use has been somewhat limited, partly due to that they do not account for between-subject *PRF* variability. In this context, Falahpour et al. (2013) proposed an alternate approach for constructing subject-specific *PRF* curves based on the global signal (GS), which is defined as the mean BOLD signal across all voxels in the brain, from each scan. Physiological regressors constructed in this way can account for a considerably larger fraction of variance in fMRI timeseries compared to the standard *PRF* curves. However, when individual *PRF* curves were used in a cross-validation analysis, the results suggested that the improvement in the explained variance may be due to overfitting (Falahpour et al., 2013).

Several data-driven approaches have been also proposed for preprocessing BOLD fMRI data. For example, in global signal regression (GSR), the GS is subtracted from the data through linear regression, implicitly assuming that processes that globally affect the fMRI BOLD signal are mostly uncorrelated to neural activity (Fox et al., 2005; Greicius et al., 2003; Qing et al., 2015). However, the validity of GSR is still under debate, as there is some evidence that the GS has a neuronal component as well (Liu et al., 2017; Murphy and Fox, 2017). Furthermore, the use of independent component analysis (ICA) or principal component analysis (PCA) to identify physiological or “noisy” components (based on their temporal, spatial and spectral features) and subsequently remove them before reconstructing the “noise-free” fMRI data, has been proposed (Churchill and Strother, 2013; Kay et al., 2013; Pruim et al., 2015; Salimi-Khorshidi et al., 2014). For example, FIX (“fMRIB’s ICA-based X-noisefier”) implements a semi-automatic procedure for denoising fMRI via classification of ICA components. Due to its performance with respect to automatic and manual classification of “noisy” components, FIX has been used in the default resting-state fMRI preprocessing pipeline for generating HCP connectomes (Salimi-Khorshidi et al., 2014). However, recent studies have demonstrated that global fluctuations captured in the GS are still prominent after FIX-denoising (Burgess et al., 2016; Power et al., 2017). Additional studies have established a strong association of the GS with slow-frequency fluctuations of respiration and heart rate (Chang and Glover, 2009a; Falahpour et al., 2013). Overall, these studies suggest that FIX, and in general PCA/ICA-based noise correction techniques, may not sufficiently correct for these noise sources.

In the present paper, we propose a novel methodological framework for extracting subject- and scan-specific *PRF* curves using the GS. We propose a double gamma structure for the *PRF* curves and a combination of optimization techniques (genetic algorithms and interior-point optimization) for parameter estimation. In contrast to previous approaches (Birn et al., 2008; Chang et al., 2009; Falahpour et al., 2013), the convolution of physiological variables (HR, breathing pattern) with the *PRF* curves is done in a pseudo-continuous time-domain at a 10 Hz sampling frequency to avoid smoothing out the effect of high-frequency physiological fluctuations of HR. In addition to between-subject variability, we rigorously investigate the between-session variability of the *PRF* curves, as well as their variability across voxels in the brain. To this end, as well as to evaluate the performance of the proposed methodology, we use resting-state fMRI data from the Human Connectome Project (HCP; Van Essen et al., 2013) collected during 4 different scanning sessions on 2 different days. The noise correction techniques discussed here are also of importance for task-based studies, such as those involving motor and pain protocols, as fluctuations in cardiac activity and breathing patterns may be time-locked to the task, and, hence, bias the results (Glasser et al., 2018).

## 85 2. Methodology

### 2.1 Human Connectome Project (HCP) Dataset

We used resting-state scans from the HCP S1200 release (Glasser et al., 2016; Van Essen et al., 2013). The HCP dataset includes, among others, resting-state (eyes-open and fixation on a cross-hair) data from healthy young (age range: 22-35 years) individuals acquired on two different days. On each day, two 15-minute scans were collected. We refer to the two scans collected on days 1 and 2 as R1a/R1b and R2a/R2b respectively. fMRI acquisition was performed with a multiband factor of 8, spatial resolution of 2 mm isotropic voxels, and a TR of 0.72 s (Glasser et al., 2013).

The minimal preprocessing pipeline for the resting-state HCP dataset is described in (Glasser et al., 2013). In brief, the pipeline includes gradient-nonlinearity-induced distortion correction, motion correction, EPI image distortion correction, non-linear registration to MNI space and mild high-pass (2000 s) temporal filtering. The motion parameters are included in the database for further correction of motion artifacts. The HCP has adopted FIX for removing structured temporal noise related to motion, non-neuronal physiology, scanner artefacts and other nuisance sources (Salimi-Khorshidi et al., 2014). FIX-denoised data are available in the HCP database as well.

In the present work, we examined minimally-preprocessed and FIX-denoised data from 41 subjects (Supplementary Table 1), which included good quality physiological signals (cardiac and respiratory waveforms) in all four scans, as assessed by visual inspection. The cardiac and respiratory signals were collected with a photoplethysmograph and respiratory belt respectively.

### 2.2 Preprocessing

Unless stated otherwise, the preprocessing and analysis described below were performed in Matlab (R2017b; Mathworks, Natick MA).

#### 2.2.1 Preprocessing of physiological recordings

The cardiac signal (i.e. photoplethysmogram) was initially band-pass filtered with a 2<sup>nd</sup> order Butterworth filter between 0.3 and 10 Hz. The minimum peak distance specified for peak detection varied between 0.5 and 0.9 seconds depending on the subject's average HR. The HR signal was computed in beats-per-minute (bpm) by multiplying the inverse of the time differences between pairs of adjacent peaks with 60, and evenly resampled at 10 Hz.

In the case of scans with abrupt changes in HR, if these changes were found by visual inspection to be due to noisy cardiac signal measurements, the HR signal was corrected for outliers using Matlab. Specifically, outliers in the HR signal were defined as the time points that deviated more than (approximately) 7 median absolute deviations (MAD) from the moving median value within a time window of 30 seconds. The MAD threshold varied across scans and was chosen empirically based on the extent of noise in the cardiac signal of each scan and the extracted HR signal. Outliers were replaced using linear interpolation (for examples of HR signals with abrupt changes and how they were treated, please see Supplementary Figs. 1 and 2).

The respiratory signal was detrended linearly and corrected for outliers using the moving median method described earlier. The duration of the moving time window and the MAD threshold were chosen separately for each scan based on visual inspection. Subsequently, the respiratory signal was low-pass filtered at 5 Hz with a 2<sup>nd</sup> order Butterworth filter and z-scored. The peak detection, used later for the extraction of RVT, was done with a minimum peak distance of 2 s and minimum peak height of 0.2.

## 125 2.2.2 Preprocessing of fMRI data

The effect of HR and respiratory variations on the fMRI BOLD signal is considered to last about half a minute (Chang et al., 2009). Therefore, the first 40 image volumes were disregarded, while the corresponding physiological data were retained. The fMRI timeseries were first spatially smoothed with a Gaussian filter of 3 mm full width at half maximum (FWHM) and then linearly detrended. Subsequently, the following nuisance variables were regressed out through linear regression: the demeaned and linearly detrended motion parameters and their derivatives, and 3<sup>rd</sup> order RETROICOR regressors for the cardiac and respiratory artifacts (Glover et al., 2000) using the physiological recordings at the original sampling rate of 400 Hz.

## 130 2.3 Physiological response functions

135 We employed linear dynamic models for extracting physiological regressors that were subsequently included in the general linear model as regressors to model the effect of the corresponding physiological variable on the BOLD signal. The physiological regressors were obtained as the convolution between the physiological variables and the corresponding PRF.

### 2.3.1 Standard cardiac response function ( $CRF_{stand}$ ; Chang et al., 2009)

140 In the present study, the model proposed in Chang et al. (2009) was considered as the standard method for removing the effect of HR fluctuations. According to this method, the HR signal is smoothed with a 6 s moving average filter before being convolved with the standard CRF ( $CRF_{stand}$ ) defined as:

$$CRF_{stand}(t) = 0.6t^{2.6}e^{-t/1.6} - 16 \frac{1}{\sqrt{2\pi(9)}} e^{-\frac{1(t-12)^2}{9}}, \quad [1.]$$

to construct the physiological regressor  $X_{HR}$  related to HR fluctuations. Finally,  $X_{HR}$  was downsampled to the fMRI sampling rate.

### 145 2.3.2 Standard respiration response function ( $RRF_{stand}$ ; Birn et al., 2008, 2006)

We used the method described in (Birn et al., 2008) as the standard method for removing the effect of changes in the breathing pattern. Briefly, the maximum and minimum peaks of each breath were initially identified on the respiratory signal and linearly interpolated at 10 Hz. Subsequently, the breathing depth was defined as the difference between the interpolated time-series of maximum and minimum peaks. The BR was calculated as the time difference between successive maximum peaks, expressed in breaths per minute (bpm; note the acronym bpm is used for both HR and BR and the distinction between them is based on the context of the sentence), and interpolated at 10 Hz. Subsequently, the respiration volume per time (RVT) was calculated as the product between breathing depth and rate. Finally, the RVT time-series were convolved with the standard RRF ( $RRF_{stand}$ ) defined as:

$$RRF_{stand}(t) = 0.6t^{2.1}e^{-t/1.6} - 0.0023t^{3.54}e^{-t/4.25} \quad [2.]$$

155 which yielded the physiological regressor  $X_{RVT}$  related to changes in the breathing pattern. Finally,  $X_{RVT}$  was downsampled to the fMRI sampling rate.

### 2.3.3 Proposed physiological response functions (PRF)

Here, we used the instantaneous HR without any smoothing, whereas the respiratory signal was first filtered with a moving average window of 1.5 s and the square of its derivative was subsequently calculated. The respiratory signal was smoothed before calculating the derivative to avoid large, physiologically implausible spikes in the extracted regressor. 160 The signal extracted after this process, termed respiratory flow (RF), reflects the absolute flow of the inhalation and exhalation of the subject at each time point. While RF carries similar information with RVT, it is expected to be more

robust as it does not depend on accurate peak detection. To reduce the time of subsequent analysis, RF was downsampled from 400 Hz to 10 Hz. Therefore, the corresponding physiological regressors were defined as follows:

$$X_{HR}(t) = HR * CRF, \text{ and} \quad [3.]$$

$$X_{RF}(t) = RF * RRF \quad [4.]$$

where  $CRF$  and  $RRF$  are the proposed cardiac and respiration response functions, respectively. The basic structure of the two proposed  $PRF$  curves was selected as the double gamma function that is also used for  $RRF_{stand}$  and the canonical hemodynamic response function (HRF) in the SPM software package (<http://www.fil.ion.ucl.ac.uk/spm/>). The gamma function is defined as:

$$\Gamma(\tau, \delta, t) = \alpha(\tau, \delta) \cdot t^{\frac{\sqrt{\tau}}{\delta}} \cdot e^{-\frac{t}{\delta\sqrt{\tau}}}, \quad [5.]$$

The parameters  $\tau$  and  $\delta$  indicate the (approximate) time of peak and dispersion of the function, and the parameter  $\alpha$  is a scaling factor which normalizes the peak value of the gamma function to 1. The  $PRF$  curves are defined as follows:

$$CRF(t) = \beta_{1,c} \cdot \Gamma(\tau_{1,c}, \delta_{1,c}, t) + \beta_{2,c} \cdot \Gamma(\tau_{2,c}, \delta_{2,c}, t), \quad [6.]$$

$$RRF(t) = \beta_{1,r} \cdot \Gamma(\tau_{1,r}, \delta_{1,r}, t) + \beta_{2,r} \cdot \Gamma(\tau_{2,r}, \delta_{2,r}, t).$$

Below, we collectively refer to the eight parameters of the gamma functions ( $\tau_{1,c}, \delta_{1,c}, \tau_{2,c}, \delta_{2,c}, \tau_{1,r}, \delta_{1,r}, \tau_{2,r}, \delta_{2,r}$ ) and the four scaling parameters ( $\beta_{1,c}, \beta_{2,c}, \beta_{1,r}, \beta_{2,r}$ ) as  $\mathbf{G}$  and  $\mathbf{B}$  respectively. Note that, since the  $PRF$  curves have arbitrary units, they can be expressed as follows:

$$CRF(t) = \beta_c [\Gamma(\tau_{1,c}, \delta_{1,c}, t) + R_c \cdot \Gamma(\tau_{2,c}, \delta_{2,c}, t)], \quad [7.]$$

$$RRF(t) = \beta_r [\Gamma(\tau_{1,r}, \delta_{1,r}, t) + R_r \cdot \Gamma(\tau_{2,r}, \delta_{2,r}, t)].$$

where the parameters  $R_c$  and  $R_r$  correspond to the ratios  $\beta_{2,c}/\beta_{1,c}$  and  $\beta_{2,r}/\beta_{1,r}$ , respectively, and the two scaling parameters  $\beta_c$  and  $\beta_r$  reflect the amount of variance explained by the corresponding physiological variables on the BOLD signal. Finally, the extracted physiological regressors were downsampled to the fMRI acquisition rate.

## 2.4 Comparison of different physiological models

Previous studies have suggested that subject-specific  $PRF$  curves may be more appropriate for constructing physiological regressors (Birn et al., 2008; Chang et al., 2009; Falahpour et al., 2013). Here, we rigorously examined this hypothesis by considering several different cases for estimating the  $PRF$  curve parameters and assessing the resulting performance. For each subject, we used four different 15-minute resting-state scans collected on two different sessions (days): R1a/R1b (day one) and R2a/R2b (day two). This allowed us to examine the variability of the  $PRF$  curves between subjects, as well as between scans and sessions of the same subject. Initially (Section 2.4.1), we considered three main models (two variants of population-specific models and a scan-specific model) to examine the variability in the shape of the  $PRF$  curves across scans for models with different degree of flexibility. Subsequently (Section 2.4.2), we assessed the performance of several variants of  $PRF$  models with respect to the explained variance to examine whether the use of subject-, session- or scan- specific  $PRF$  is justifiable. In both cases, the GS from each scan was used to define the  $PRF$  curves and assess model performance. To extend these results (Section 2.4.3), we compared the performance of a subset of the models considered in 2.4.2 as well as the performance of a voxel-specific model in individual voxels.

### 2.4.1 Variability in the shape of the $PRF$ curves across scans

Here, we aimed to examine the variability in the shape of  $PRF$  curves across scans for models based on different degree of flexibility. In addition, we aimed to understand the relation of the variability in shape to physiological variables such as the mean HR. To this end, we examined three variants of the proposed  $PRF$  curves, termed  $PRF_{ppl}$ ,  $PRF_{ppl}^{sc}$  and  $PRF_{sc}$

that were used to explain fluctuations on the GS of each scan. The  $PRF_{ppl}$  population-specific model is based on Eq. 7  
195 and is the least flexible model, as it assumes that  $\mathbf{G}$  (i.e.,  $\tau_{1,c}, \delta_{1,c}, \tau_{2,c}, \delta_{2,c}, \tau_{1,r}, \delta_{1,r}, \tau_{2,r}, \delta_{2,r}$ ) and  $\mathbf{R}$  (i.e.,  $R_c, R_r$ ) are the same for all subjects. In this model, only  $\mathbf{B}$  (i.e.,  $\beta_c, \beta_r$ ), which determines the amount of variance explained by HR and breathing pattern on the GS for each scan, was allowed to vary across scans. The  $PRF_{ppl}^{SC}$  model is also a population-specific model that allows variability in the shape of the  $PRF$  curves between scans. Specifically, it is based on Eq. 6  
200 and it assumes that  $\mathbf{G}$  ( $\tau_{1,c}, \delta_{1,c}, \tau_{2,c}, \delta_{2,c}, \tau_{1,r}, \delta_{1,r}, \tau_{2,r}, \delta_{2,r}$ ) is the same for all subjects while  $\mathbf{B}$  (i.e.,  $\beta_{1,c}, \beta_{2,c}, \beta_{1,r}, \beta_{2,r}$ ) was allowed to vary across scans. However, in this case,  $\mathbf{B}$  determines both the amount of variance explained by the physiological variables on the GS as well as the shape of the  $PRF$  curves. Finally,  $PRF_{sc}$  is a scan-specific model also based on Eq. 6, in which all the parameters were allowed to vary across scans. The  $PRF$  parameters were estimated with the non-linear optimization techniques described in Section 2.4.1.1.

In the case of the scan-specific model  $PRF_{sc}$ , apart from comparing the curves with their standard counterparts and  
205 population-specific curves  $PRF_{ppl}$ , we also examined whether the physiological variables for each scan can explain the between-scan variability in the shape of the curves as well as the performance with respect to the explained variance on the GS. Specifically, we examined whether the mean and variance of HR and BR/RF were correlated with the time of positive and negative peaks for  $CRF_{sc}$  and  $RRF_{sc}$ , respectively. In addition, we examined whether the mean and variance of HR and BR/RF were correlated to the correlation coefficient values between the corresponding physiological  
210 regressors (Eqs. 3-4) and the GS. Overall, we examined the relationship of 18 pairs of variables consisting of 6 explanatory variables, the mean and variance of HR, BR and RF, and 6 dependent variables, the time of positive and negative peak of the  $CRF_{sc}/RRF_{sc}$  curves as well as the correlation coefficient between the corresponding physiological regressors and the GS. Pairs of variables related to both HR and breathing pattern (e.g. mean of HR and time of positive peak for  $RRF_{sc}$ ) were not considered. Regarding statistical testing, we used an alpha level of .05 adjusted for multiple  
215 comparisons (N=18) with Bonferroni correction.

#### 2.4.1.1 $PRF$ parameter estimation

The parameters of the population-specific model  $PRF_{ppl}$  were estimated as follows (for a pseudocode of the algorithm, please see Supplementary Table 2): 1. for a set of given parameters, the two  $PRF_{ppl}$  curves were constructed. Subsequently, for each scan, 2. the HR and RF signals (sampled at 10 Hz) were convolved with  $CRF_{ppl}$  and  $RRF_{ppl}$   
220 respectively to extract the corresponding physiological regressors and then downsampled to match the fMRI acquisition rate. 3. Estimation of general linear model (GLM) was performed, whereby the GS was the dependent variable and the two physiological regressors were the two explanatory variables. 4. the Pearson correlation coefficient between the GS and the model prediction was calculated. 5. after performing steps 1-4 for all scans, the correlation value was averaged across all scans and returned by the algorithm and 6. the parameter values that maximized this correlation value were  
225 estimated using numerical optimization techniques as described later.

In the case of  $PRF_{ppl}^{SC}$ , steps 2 and 3 were implemented as follows: In step 2, the two gamma functions for each  $PRF_{ppl}^{SC}$   
curve were convolved separately with HR and RF. As a result, in step 3, two physiological regressors related to HR and two regressors related to RF were included in the GLM as explanatory variables (for a pseudocode of the algorithms for the  $PRF_{ppl}$  and  $PRF_{ppl}^{SC}$  models, please see Supplementary Table 2). Finally, the procedure described above was followed  
230 for the estimation of the parameters in the scan-specific model  $PRF_{sc}$ , with the only difference being that step 5 was omitted, as the  $PRF_{sc}$  parameters were estimated separately for each scan.

To obtain the optimal parameter values for the  $PRF_{ppl}$  model, a genetic algorithm (GA) implemented in Matlab R2017b's Global Optimization Toolbox was initially applied. GAs are a family of popular heuristic optimization techniques that search the parameter space for the optimal solution of a problem in a manner inspired by Darwin's principle of natural  
235 selection (Holland, 1975). GAs have generally higher demands in CPU time compared to gradient-based algorithms, but they are capable of providing potentially global optimal solutions for complex functions (Patel and Padhiyar, 2015). The parameters  $\boldsymbol{\tau}$  ( $\tau_{1,c}, \tau_{2,c}, \tau_{1,r}, \tau_{2,r}$ ) and  $\boldsymbol{\delta}$  ( $\delta_{1,c}, \delta_{2,c}, \delta_{1,r}, \delta_{2,r}$ ) were bounded between 0-20 seconds and 0-3 seconds,

respectively. A stopping criterion of 100 generations was set, as it was found to be adequate for convergence. The solution of the GA was subsequently used as the initial point for the interior-point gradient-based algorithm, also implemented in  
240 Matlab R2017b (Optimization Toolbox), with a stopping criterion of 100 maximum iterations, to refine the solution.

To accelerate the estimation procedure for the remaining models, the obtained  $PRF_{ppl}$  parameter values (or curves) were used as the initial point for all models and the interior-point algorithm was employed with a stopping criterion of 100 maximum iterations to refine the solution. Moreover, since the parameter estimation for the scan-specific models was performed using a smaller amount of data, making these models more prone to overfitting, the upper and lower  
245 boundaries for  $\tau$  and  $\delta$  were restricted to non-negative numbers ( $\pm 3$  sec compared to the population-specific  $PRF_{ppl}$  model parameter values).

#### 2.4.2 Comparison of population-, subject-, session- and scan-specific PRF curves

This section aimed to assess the performance of 13 different models (Table 1) with respect to the explained variance using two-level cross-validation (CV) to examine whether  $PRF$  curves significantly vary between subjects as well as  
250 between sessions or scans within-subject. For each model, the  $PRF$  parameters were estimated from one segment of data (training set at the first-level of CV; 3<sup>rd</sup> column of Table 1) and model performance was assessed in a separate segment of data (validation set at the first-level of CV; 4<sup>th</sup> column of Table 1) as described in sections 2.4.2.1 and 2.4.2.2, respectively.

##### 2.4.2.1 PRF parameter estimation at the first-level of cross-validation

The  $PRF$  models listed in Table 1 are, to some extent, sorted by the least to the most flexible model. The first six models ( $PRF_{ppl}$  to  $PRF_{sbj,sdd}$ ) are based on Eq. 7. In this case,  $\mathbf{R}$  ( $R_c, R_r$ ), along with  $\mathbf{G}$  ( $\tau_{1,c}, \delta_{1,c}, \tau_{2,c}, \delta_{2,c}, \tau_{1,r}, \delta_{1,r}, \tau_{2,r}, \delta_{2,r}$ ), define the shape of the  $PRF$  curves; they were assumed to be population-specific for  $PRF_{ppl}$  and subject-specific for models  $PRF_{sbj,d}$  to  $PRF_{sbj,sdd}$ . In these models,  $\mathbf{B}$  ( $\beta_c, \beta_r$ ) reflects the amount of explained variance of each  
260 physiological variable on the GS. The last 7 models ( $PRF_{ppl}^{sc}$  to  $PRF_{sc}$ ) are based on Eq. 6. The  $PRF_{ppl}^{sc}$  model assumes that  $\mathbf{G}$  is population-specific, the models  $PRF_{sbj,d}^{sc}$  to  $PRF_{sbj,sdd}^{sc}$  assume that  $\mathbf{G}$  is subject-specific, while the  $PRF_{sc}$  model assumes that it is scan-specific. In the last seven models  $\mathbf{B}$  ( $\beta_{1,c}, \beta_{2,c}, \beta_{1,r}, \beta_{2,r}$ ) defines the amount of explained variance of the physiological variables on the GS as well as the shape of the  $PRF$  curves. As described in Section 2.4.1, in all 13 models, the interior-point gradient-based algorithm was applied after being initialized with the parameter values obtained  
265 from the population-specific model  $PRF_{ppl}$  (for a pseudocode of the algorithm used to estimate the  $PRF$  parameters in all 13 models, please see Supplementary Table 2).

The following notation was adopted: the subscript in the six models  $PRF_{ppl}$  to  $PRF_{sbj,sdd}$  (Table 1) indicates whether  $\mathbf{G}$  and  $\mathbf{R}$  were estimated from the entire *population* ('ppl') or a different scan of the same *subject* ('sbj'). The letters 'd' and 's' in the subscript indicate whether parameter estimation and model performance assessment were implemented  
270 using data from one or more scans collected during a *different* or the *same* scanning session. For example,  $PRF_{sbj,dd}$  denotes that  $\mathbf{G}$  and  $\mathbf{R}$  were estimated using data from two scans collected during one session (e.g. R1a/R1b) and model performance was assessed using data from a scan collected during a different session (e.g. R2a) from the same subject. Similarly, the subscript in the seven models  $PRF_{ppl}^{sc}$  to  $PRF_{sbj,sdd}^{sc}$  indicates whether  $\mathbf{G}$  was estimated from the entire *population* ('ppl'), a different scan of the same *subject* ('sbj') or the same *scan* ('sc') with respect to the scan that the model performance was assessed on. In addition, the superscript 'sc' in the six models  $PRF_{ppl}^{sc}$  to  $PRF_{sbj,sdd}^{sc}$  (Table 1) indicates that, even though  $\mathbf{G}$  may be population- or subject-specific, the ultimate  $PRF$  shape is different for each *scan*. This is due to that  $\mathbf{B}$ , which was estimated for each scan separately, in the six models  $PRF_{ppl}^{sc}$  to  $PRF_{sbj,sdd}^{sc}$ , consists of four parameters (i.e.,  $\beta_{1,c}, \beta_{2,c}, \beta_{1,r}, \beta_{2,r}$ ), in contrast to the first 6 models for which  $\mathbf{B}$  consists of two parameters (i.e.,  $\beta_c, \beta_r$ ), allowing some flexibility in the shape of the  $PRF$ . Finally, the subscript 'sc' for the last model ( $PRF_{sc}$ )



**Table 1.** Assessment of the performance of population-, subject-, session- and scan- specific *PRF* models using two-level cross-validation (*CV*; *stand*: standard, *ppl*: population, *sbj*: subject, *sc*: scan, *d*: different, *s*: same)

<b>Model:</b>	<b>Estimated <i>PRF</i> parameters (non-linear optimization):</b>	<b>Obtained from (training set at the first-level of CV):</b>	<b>Model performance assessed on (validation set at the first-level of CV):</b>	<b>Estimated linear regression parameters (<i>B</i>):</b>
$PRF_{stand}$	---	Eqs. 1 and 2	any scan	$\beta_c, \beta_r$
$PRF_{ppl}$	$\tau_{1,c}, \delta_{1,c}, \tau_{2,c}, \delta_{2,c}, R_c,$ $\tau_{1,r}, \delta_{1,r}, \tau_{2,r}, \delta_{2,r}, R_r$	entire population - leave one out cross-validation (LOOCV; e.g. estimate parameters from set of subjects $\mathbf{S}^t = \{S_1, S_2, \dots, S_{i-1}, S_{i+1}, S_{i+2}, \dots, S_{41}\}$ when the model performance is assessed for subject $S_i$ )	any scan of subject $S_i$	same as $PRF_{stand}$
$PRF_{sbj,d}$	same as $PRF_{ppl}$	one scan; scan $R_{i\{a,b\}}$ of subject $S_x$	scan $R_{j\{a,b\}}$ from <i>different</i> session (day) of subject $S_x$ where $i \neq j$	same as $PRF_{stand}$
$PRF_{sbj,dd}$	same as $PRF_{ppl}$	two scans of a session; scans $R_{i,a}$ & $R_{i,b}$ of subject $S_x$ where $i = \{1,2\}$	scan $R_{j\{a,b\}}$ from <i>different</i> session of subject $S_x$ where $j = \{1,2\}$ and $i \neq j$	same as $PRF_{stand}$
$PRF_{sbj,s}$	same as $PRF_{ppl}$	one scan; scan $R_{i,j}$ of subject $S_x$ where $i = \{1,2\}$ and $j = \{a,b\}$	scan $R_{i,k}$ from <i>same</i> session of subject $S_x$ where $k = \{a,b\}$ and $j \neq k$	same as $PRF_{stand}$
$PRF_{sbj,sd}$	same as $PRF_{ppl}$	one scan of each session; scans $R_{i,j}$ & $R_{k\{a,b\}}$ of subject $S_x$ where $i = \{1,2\}$ , $j = \{a,b\}$ , $k = \{1,2\}$ and $i \neq k$	a different scan $R_{i,l}$ of subject $S_x$ where $l = \{a,b\}$ and $j \neq l$	same as $PRF_{stand}$
$PRF_{sbj,sdd}$	same as $PRF_{ppl}$	three scans; scans $R_{i,j}$ , $R_{k,a}$ and $R_{k,b}$ of subject $S_x$ where $i = \{1,2\}$ , $j = \{a,b\}$ , $k = \{1,2\}$ and $i \neq k$	a different scan $R_{i,l}$ of subject $S_x$ where $l = \{a,b\}$ and $j \neq l$	same as $PRF_{stand}$
$PRF_{ppl}^{sc}$	$\tau_{1,c}, \delta_{1,c}, \tau_{2,c}, \delta_{2,c},$ $\tau_{1,r}, \delta_{1,r}, \tau_{2,r}, \delta_{2,r}$	entire population - leave one out cross-validation (LOOCV; e.g. estimate parameters from set of subjects $\mathbf{S}^t = \{S_1, S_2, \dots, S_{i-1}, S_{i+1}, S_{i+2}, \dots, S_{41}\}$ when the model performance is assessed for subject $S_i$ )	any scan of subject $S_i$	$\beta_{1,c}, \beta_{2,c},$ $\beta_{1,r}, \beta_{2,r}$
$PRF_{sbj,d}^{sc}$	same as $PRF_{ppl}^{sc}$	one scan; scan $R_{i\{a,b\}}$ of subject $S_x$ where $i = \{1,2\}$	scan $R_{j\{a,b\}}$ from <i>different</i> session of subject $S_x$ where $i \neq j$	same as $PRF_{pop}^{sc}$
$PRF_{sbj,dd}^{sc}$	same as $PRF_{ppl}^{sc}$	two scans of a session; scans $R_{i,a}$ & $R_{i,b}$ of subject $S_x$ where $i = \{1,2\}$	scan $R_{j\{a,b\}}$ from <i>different</i> session of subject $S_x$ where $i \neq j$	same as $PRF_{pop}^{sc}$
$PRF_{sbj,s}^{sc}$	same as $PRF_{ppl}^{sc}$	one scan; scan $R_{i,j}$ of subject $S_x$ where $i = \{1,2\}$ and $j = \{a,b\}$	scan $R_{i,k}$ from <i>same</i> session of subject $S_x$ where $k = \{a,b\}$ and $j \neq k$	same as $PRF_{ppl}^{sc}$
$PRF_{sbj,sd}^{sc}$	same as $PRF_{ppl}^{sc}$	one scan of each session; scans $R_{i,j}$ & $R_{k\{a,b\}}$ of subject $S_x$ where $i = \{1,2\}$ , $j = \{a,b\}$ , $k = \{1,2\}$ and $i \neq k$	a different scan $R_{i,l}$ of subject $S_x$ where $l = \{a,b\}$ and $j \neq l$	same as $PRF_{ppl}^{sc}$
$PRF_{sbj,sdd}^{sc}$	same as $PRF_{ppl}^{sc}$	three scans; scans $R_{i,j}$ , $R_{k,a}$ and $R_{k,b}$ of subject $S_x$ where $i = \{1,2\}$ , $j = \{a,b\}$ , $k = \{1,2\}$ and $i \neq k$	a different scan $R_{i,l}$ of subject $S_x$ where $l = \{a,b\}$ and $j \neq l$	same as $PRF_{ppl}^{sc}$
$PRF_{sc}^{sc}$	same as $PRF_{ppl}^{sc}$	one scan; scan $R_{i,j}$ of subject $S_x$ where $i = \{1,2\}$ and $j = \{a,b\}$	the same scan $R_{i,j}$ of subject $S_x$	same as $PRF_{ppl}^{sc}$

280 indicates that both  $\mathbf{G}$  and  $\mathbf{B}$  were estimated and validated from data collected during the same scan; therefore, this was the most flexible model (for schematic examples of training and validation sets for each model, please see Supplementary Fig. 3).

To assess the performance of the population-specific models  $PRF_{ppl}$  and  $PRF_{ppl}^{sc}$ , a leave-one-out cross-validation (LOOCV) approach was implemented at the first-level, whereby the  $PRF$  curves were obtained using training data from 40 subjects and validated with data from the remaining subject. In the case of subject-specific models of the form  $PRF_{sbj,x}^x$ , we considered all possible scan combinations (instead of using only one of the scans as the validation data set) to examine the effect of session on the variability of  $PRF$  curves (e.g.  $PRF_{sbj,d}$  vs  $PRF_{sbj,s}$ ) as well as the dependence of the model performance on the amount of training data (e.g.  $PRF_{sbj,d}$  vs  $PRF_{sbj,dd}$ ) in more detail.

#### 2.4.2.2 Assessment of model performance

290 For a given scan and model, the  $PRF$  parameters ( $\mathbf{G}$  and  $\mathbf{R}$ ) were extracted at the first-level as described earlier (Section 2.4.2.1). Subsequently, at the second-level, a 3-fold cross validation approach was implemented using the validation set of the first-level to prevent overfitting. Each scan in the validation set of the first-level CV was partitioned into three segments of about 5 minutes each. One segment was used as the validation set at the second-level for assessing the performance of the model and the remaining two segments were used as the training dataset (at the second-level). This step was repeated three times with each of the three segments used exactly once as the validation data. In each fold, linear regression analysis was performed on the training set to estimate  $\mathbf{B}$  (5<sup>th</sup> column of Table 1). Subsequently, the estimated  $\mathbf{B}$  was used on the validation set (second-level), and the correlation of the model prediction with the GS was calculated. Finally, the mean correlation across the three folds was calculated. For the  $PRF_{sc}$  model, one-level cross-validation was used. Specifically, the estimation of both  $\mathbf{G}$  and  $\mathbf{B}$  was performed on the training set of each fold (i.e., two segments of 300 5 minutes) and subsequently used on the validation dataset (i.e., the remaining segment of that scan).

For each model, the  $PRF$  parameters and performance assessment can be obtained from different scan combinations. For instance, in the case of  $PRF_{sbj,d}$  for a given subject, the  $PRF$  parameters can be estimated from scans R1a (or R1b) and the performance can be assessed on scans R2a (or R2b), yielding 8 total combinations. Therefore, for a given subject, the final performance of a model was assessed for all possible combinations and the average of the obtained values was used at the group level to compare the performance between all examined models (Table 1).

#### 2.4.2.3 Effect of sample size and duration of scan on $PRF$ parameter estimation

To investigate the effect of the number of subjects on parameter estimation in population-specific models ( $PRF_{ppl}$  and  $PRF_{ppl}^{sc}$ ), we repeated the assessment of model performance for the models  $PRF_{ppl}$  and  $PRF_{ppl}^{sc}$  for the following subject numbers: 1-10, 15, 20, 25, 35 and 40. The subjects were randomly chosen and this part of the analysis was repeated ten times to eliminate biases from “representative” or “non-representative” subjects chosen in a particular iteration. Similarly, to examine the effect of scan duration on the estimation of  $PRF$  parameters and investigate the minimum required duration in scan-specific models, we evaluated the performance of the models  $PRF_{ppl}$  and  $PRF_{sc}$  for scan durations between 1 to 15 minutes in steps of one minute.

#### 315 2.4.3 Comparison of population-, scan- and voxel-specific $PRF$ curves in individual voxels

Here, we aimed to examine the variability of the  $PRF$  curves across voxels. To this end, we compared the performance of a subset of models considered in 2.4.2, particularly the standard models  $PRF_{stand}$ , the  $PRF_{ppl}$ ,  $PRF_{ppl}^{sc}$  and  $PRF_{sc}$  models, in individual voxels. In addition, we examined the performance of a voxel-specific  $PRF$  model, termed  $PRF_{sc}^{vxl}$ .  $PRF_{sc}^{vxl}$  was simply an extension of  $PRF_{sc}$  that allowed variability in the shape of the  $PRF$  curve across voxels. The  $PRF$  curves for the first four models (standard models  $PRF_{stand}$ ,  $PRF_{ppl}$ ,  $PRF_{ppl}^{sc}$  and  $PRF_{sc}$ ) were estimated based on the 320

325 GS of one or more scans as described earlier in Section 2.4.2. These curves were subsequently used to extract two physiological regressors that were included in the GLM for a voxel-wise analysis. On the other hand, for the  $PRF_{sc}^{vxl}$  model, the four gamma functions corresponding to parameters  $\mathbf{G}$  and  $\mathbf{B}$  of  $PRF_{sc}$  were used to extract four physiological regressors for the GLM. Due to that  $PRF_{sc}^{vxl}$  had more physiological regressors in the GLM than the other models examined in this section (4 vs 2), a 3-fold cross validation approach was implemented to assess model performance as described in Section 2.4.2.1.

330 The comparison of the models was restricted to regions of interest (ROIs) where the models explained significant variance. Specifically, these ROIs were defined for each model separately and included the 5% of voxels in the brain with the highest correlation between the voxel timeseries and the prediction of the corresponding model. The aforementioned five  $PRF$  models were examined for  $CRF$  and  $RRF$  separately as well as both  $CRF$  and  $RRF$ , yielding 15 models in total. The comparison between the 15 models was repeated on FIX-denoised data using ROIs for each model the ones derived from the original data. Finally, to examine the effect of spatial smoothing on the performance of  $PRF$  models, the comparison between the 15 models on the raw data was performed with a FWHM value of 0 mm and 6 mm in addition to the value of 3 mm used for the main analysis.

335 For visualization purposes, the statistical maps shown here were overlaid on structural images after being transformed to structural space with FSL's FLIRT registration tool (Jenkinson and Smith, 2001) as incorporated in the MANGO software (Lancaster, Martinez; [www.ric.uthscsa.edu/mango](http://www.ric.uthscsa.edu/mango)).

### 3. Results

#### 3.1 Variability in physiological measurements

The mean HR and BR values during resting conditions exhibited considerable variability across the 164 scans, with the mean HR and BR ranging between 46-106 bpm and 13-23 bpm, respectively. To examine the variability across subjects and sessions, all scans were grouped in pairs a) from different subjects ( $N = 13120$ ; for a pair of scans the first scan was picked from all 164 scans and the second scan from the 160 scans of the remaining 40 subjects. Thus, the number of unique pairs was  $164 \times 160$  divided by two as the order does not matter), b) from different sessions of the same subject ( $N = 41 \cdot 2 \cdot 2 = 164$ ), and c) from scans of the same session ( $N = 41 \cdot 2 = 82$ ). The mean HR differences obtained from the scan pairs in groups a, b and c yielded standard deviation values of 16, 8 and 2 bpm respectively, and the corresponding variance values were found to be significantly different ( $F$ -test;  $p$ -value:  $<10^{-49}$ ). Similarly, the differences in BR obtained from the scan pairs in groups a, b and c yielded standard deviation values of 3.1, 1.7 and 1.0 bpm, and the corresponding variance values were found again to be significantly different ( $F$ -test;  $p$ -value:  $<10^{-15}$ ). In other words, the between subject variability in mean HR and BR was significantly larger compared to the within-subject variability and, in turn, the between session within-subject variability was larger than the within session variability. In Fig. 1, we show the variability of mean HR and BR across subjects, sessions and scans for 10 representative subjects, which illustrates the aforementioned statistical differences. For instance, significant differences were found between scans of different subjects such as in the case of subjects S406432 (light blue color) and S555348 (brown color), whereby all four scans of the former subject are characterized by lower mean HR and BR compared to the four scans of the latter one. Also, significant variability is found between sessions within-subject such as in the case of subject S203923 (cyan color) whereby both mean HR and BR increase from the first to the second session.

#### 3.2 Variability in the shape of $PRF$ curves across scans

This section examines the variability in the shape of the  $PRF_{ppl}$ ,  $PRF_{ppl}^{sc}$  and  $PRF_{sc}$  curves. For all 164 scans examined in this study, it was found that the GS was strongly correlated to cardiac and respiratory activity. The first column of Fig. 2 shows the optimal  $CRF_{ppl}$  and  $RRF_{ppl}$  curves estimated for the 41 subjects using the  $PRF_{ppl}$  model that assumes the same  $CRF$  and  $RRF$  for the entire population. Both the  $PRF_{stand}$  and  $PRF_{ppl}$  curves have a bimodal shape with a positive peak followed by a negative one. However, the amplitude and time of the peaks differ between the curves. The peaks in the  $CRF_{ppl}$  appear at much earlier time lags compared to  $CRF_{stand}$  (Chang et al., 2009; 1.2 and 7.0 s for  $CRF_{ppl}$ , vs. 4.1 and 12.4 s for  $CRF_{stand}$ ). Faster dynamics were also observed in the estimated  $RRF_{ppl}$  compared to  $RRF_{stand}$  (Birn et al., 2008). Specifically, the positive and negative peaks of the  $RRF_{ppl}$  were found to be located at 2.0 and 12.8 s,

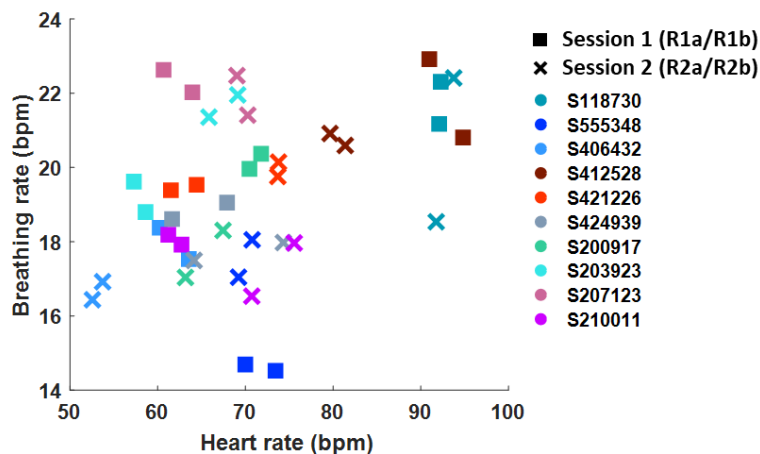


**Fig. 1. Scatterplot of mean heart rate (HR) and breathing rate (BR) from scans of 10 representative subjects.** Squares and crosses correspond to scans from sessions (days) 1 and 2, respectively, whereas each color indicates a different subject. Both mean HR and BR vary less across scans of the same session than scans across different sessions within-subject. In turn, mean HR and BR across the four scans of each subject exhibited lower variability compared to scans from different subjects.

**Table 2. Parameters for the  $PRF_{ppl}^{(sc)}$  model.** The parameters  $\tau$  and  $\delta$  used in Eq. 5 are an approximate measure for the time of peak and dispersion of the gamma function. The full width at half maximum (FWHM) was calculated numerically.

	$CRF_{ppl}^{(sc)}$		$RRF_{ppl}^{(sc)}$	
	$\Gamma_{c_1}(t)$	$\Gamma_{c_2}(t)$	$\Gamma_{r_1}(t)$	$\Gamma_{r_2}(t)$
Time to peak $\tau$ (s)	3.1	5.6	1.9	12.5
Dispersion $\delta$ (s)	2.5	0.9	2.9	0.5
FWHM (s)	9.2	8.3	7.0	11.1
Ratio $R$ ( $\beta_2/\beta_1$ ) (only for $PRF_{ppl}$ )	N/A	-1.1	N/A	-2.6

respectively, whereas the corresponding peaks in the  $RRF_{stand}$  are at 3.1 and 15.5 s. Moreover, the estimated  $PRF_{ppl}$  curves return to baseline faster than the corresponding  $PRF_{stand}$  curves. Finally,  $CRF_{ppl}$  and  $RRF_{ppl}$  exhibited a stronger positive and negative peak respectively compared to the standard curves (factor of  $\sim 2$ ).

The second column of Fig. 2 shows the gamma functions that were used to construct the  $PRF_{ppl}$  and  $PRF_{ppl}^{sc}$  curves while the third column presents scatterplots of  $\mathbf{B}$  ( $\beta_{c_1}, \beta_{c_2}, \beta_{r_1}, \beta_{r_2}$ ), which defined the shape of the  $CRF_{ppl}^{sc}$  and  $RRF_{ppl}^{sc}$  curves, for all scans. Specifically,  $\beta_{c_1}$  ( $\beta_{r_1}$ ) and  $\beta_{c_2}$  ( $\beta_{r_2}$ ) correspond to the sign and magnitude of the first and second peak of the  $CRF_{ppl}^{sc}$  ( $RRF_{ppl}^{sc}$ ) curve, respectively. The parameters of the four gamma functions are listed in Table 2. All parameters in  $\mathbf{B}$  for  $CRF_{ppl}^{sc}$  are located on the 4<sup>th</sup> quadrant (Fig. 2c) and can be approximated well with a straight line that crosses the origin of the plane with a slope  $R$  of -1.1. However, the small deviation of each circle from the straight line suggests that the  $CRF_{ppl}^{sc}$  curves had small differences compared to the  $CRF_{ppl}$  curve shown in Fig. 2b. Furthermore,

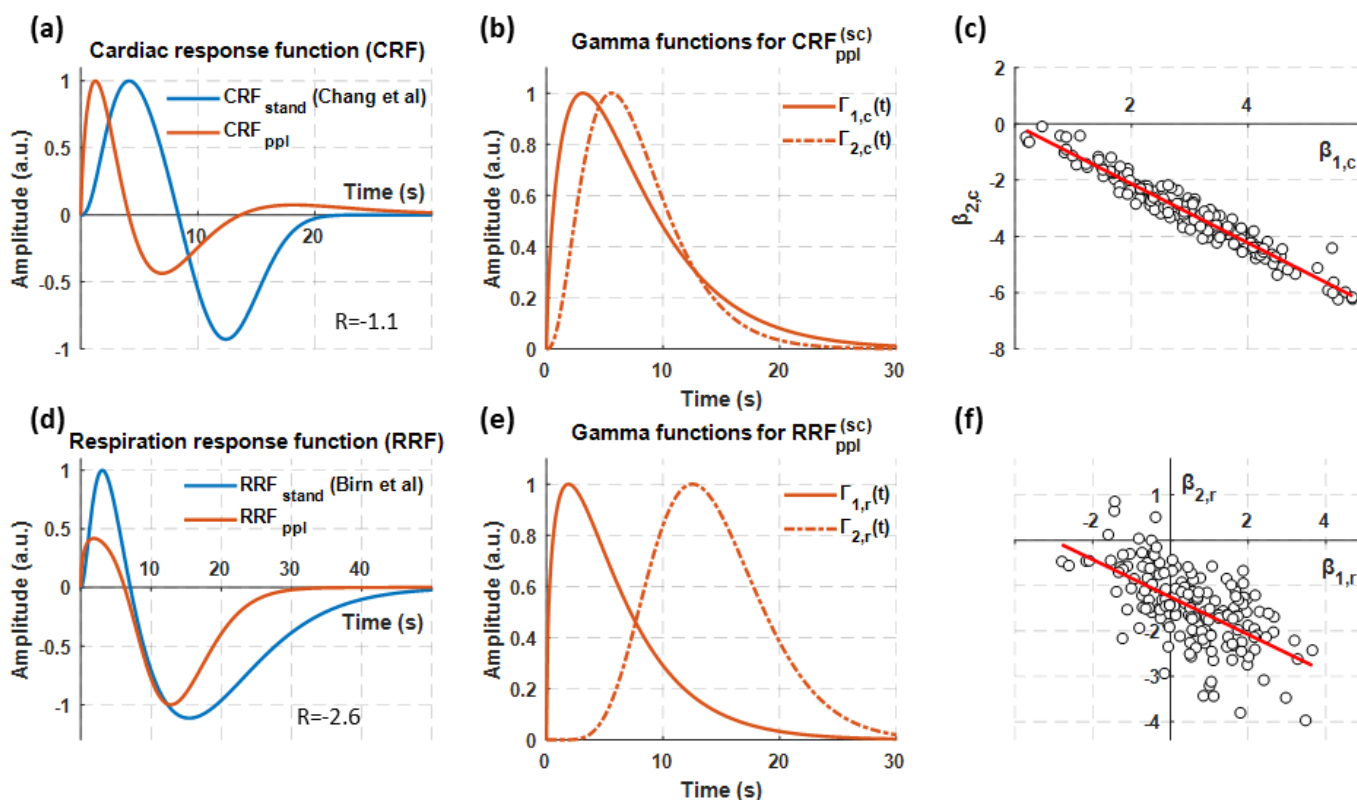
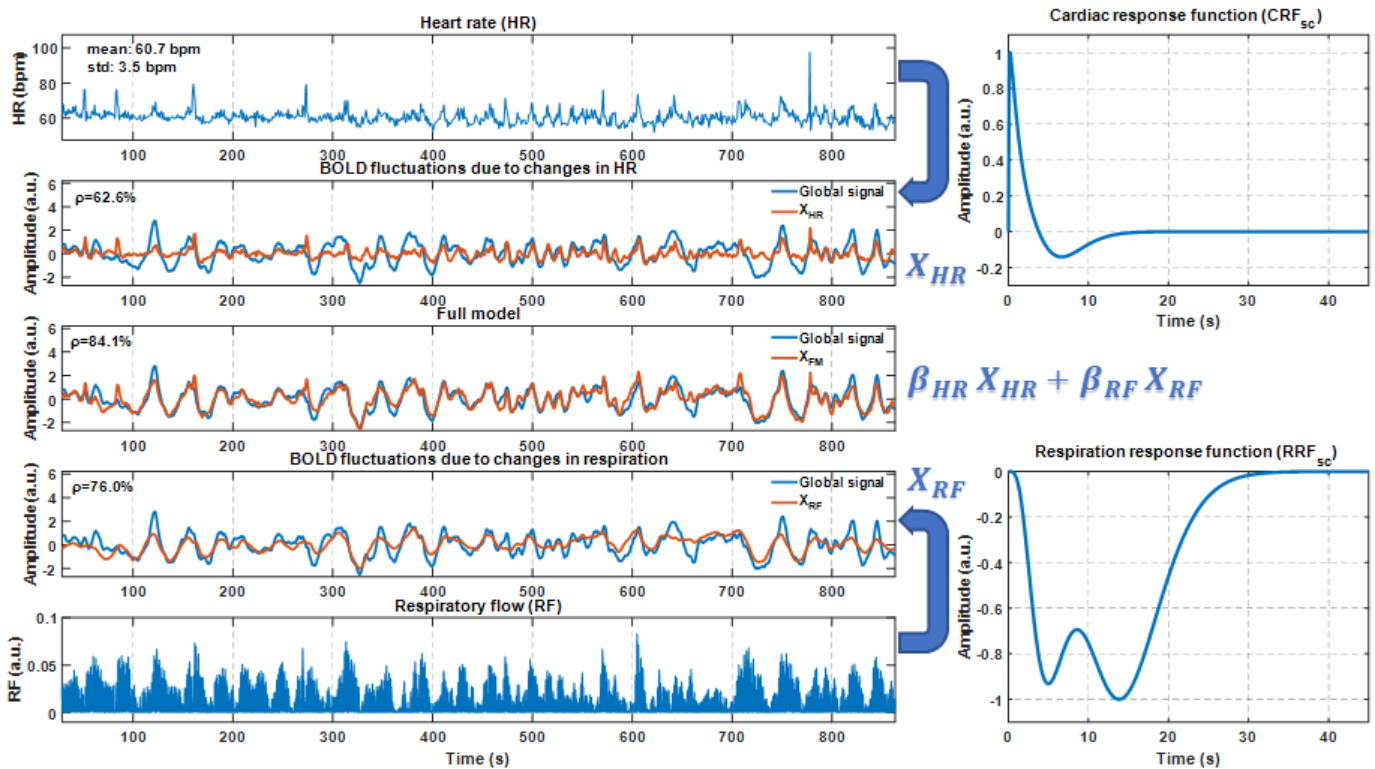


**Fig. 2. Estimated gamma functions for the  $CRF_{ppl}^{(sc)}$  and  $RRF_{ppl}^{(sc)}$  curves.** (a) Standard  $CRF_{stand}$  and estimated  $CRF_{ppl}$  curves. (b) The two gamma functions used to construct the population-specific  $CRF_{ppl}$  and  $CRF_{ppl}^{sc}$  curves. (c) Scatterplot of parameters in  $\mathbf{B}$  for the  $CRF_{ppl}^{sc}$  model. The circles correspond to the 164 scans and the values of  $\beta_{1,c}$  and  $\beta_{2,c}$  reflect the amplitude of the gamma functions  $\Gamma_{1,c}$  and  $\Gamma_{2,c}$  shown in (b). In a similar manner, (d), (e) and (f) illustrate the results for the models related to  $RRF$ .

### Subject: 210415 (R1a)



### Subject: 307127 (R2a)

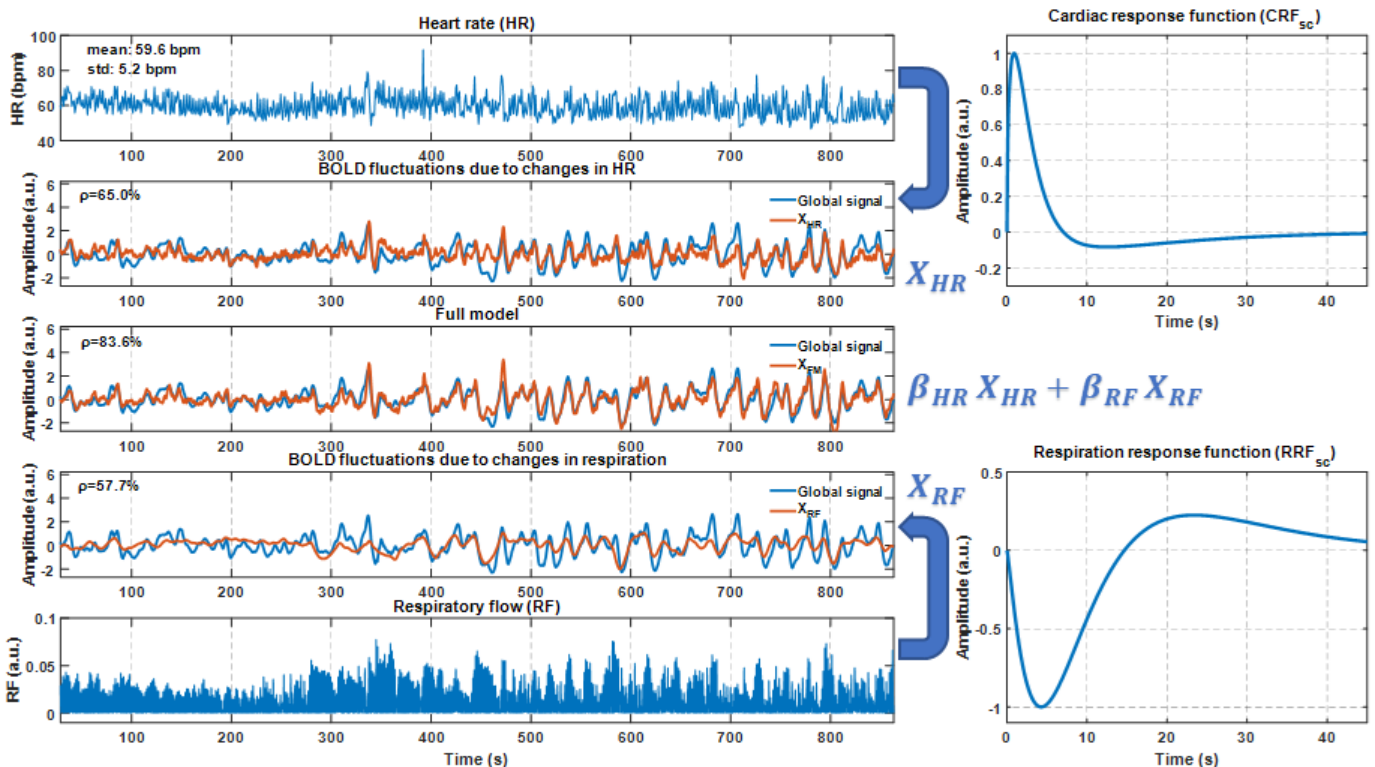


**Fig. 3. Demonstration of the  $PRF_{sc}$  model performance for two subjects.** The HR (1<sup>st</sup> row of each subject's panel) and RF (5<sup>th</sup> row) time series were derived from the recorded physiological signals (photoplethysmograph and respiratory belt, respectively). Subsequently, the scan-specific curves  $CRF_{sc}$  and  $RRF_{sc}$  were obtained after estimating the corresponding  $PRF$  parameters (right column). The physiological regressors  $X_{HR}$  and  $X_{RF}$  shown in the 2<sup>nd</sup> and 4<sup>th</sup> row respectively were obtained as the convolution between HR/RF with  $CRF_{sc}/RRF_{sc}$ . The parameters  $\beta_{HR}$  and  $\beta_{RF}$  were estimated by maximizing the variance of the GS explained by the model (3<sup>rd</sup> row).

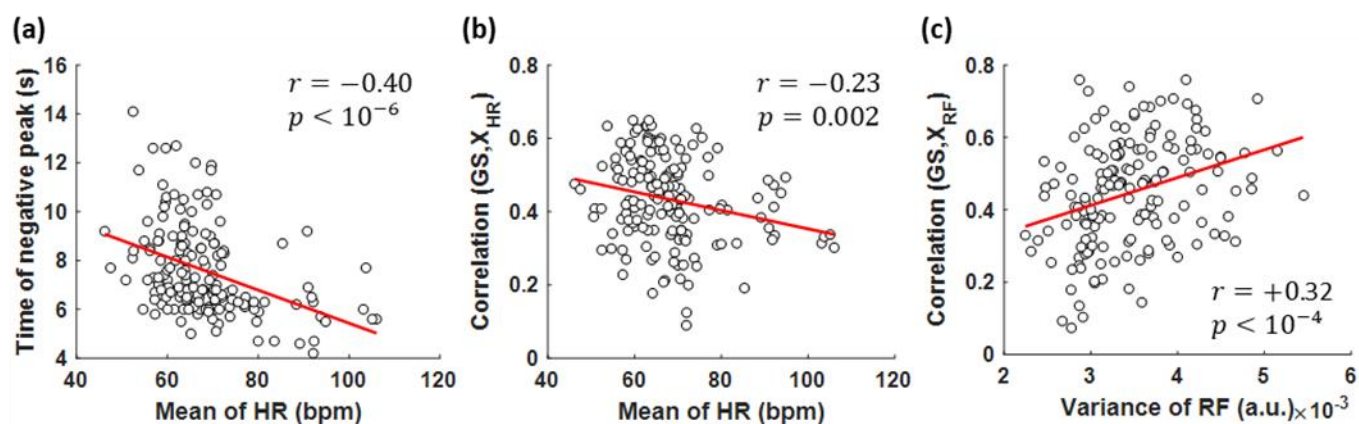


**Fig. 4. Scatterplots of physiological variables and features from the  $PRF_{sc}$  models.** (a) The time-to-peak values for the negative  $CRF_{sc}$  peak were negatively correlated with mean HR. (b) The mean HR was negatively correlated with the correlation coefficient between the cardiac regressor  $X_{HR}$  and GS. (c) The variance of RF was strongly correlated with the correlation coefficient between the respiratory regressor  $X_{RF}$  and GS.

the parameters in **B** for the  $RRF_{ppl}^{sc}$  curves (Fig. 2f) indicate an even larger variability of the curves across scans compared to the  $RRF_{ppl}$  shown in Fig. 2e.

Fig. 3 illustrates the estimated  $PRF_{sc}$  curves for two subjects that demonstrated strong association between the GS with both HR and breathing patterns. It also shows the physiological variables HR and RF, as well as the estimated regressors that maximized the correlation with the GS. For the majority of the examined subjects, including the two subjects whose results are shown in Fig. 3, it was observed that HR explains faster fluctuations of the GS compared to RF. Additionally, we observe that even though the two subjects had almost the same mean HR, the corresponding dynamic patterns were very different. Specifically, the HR of subject 210415 was relatively stable with sporadic abrupt increases whereas the HR of subject 30717 exhibited faster fluctuations. With respect to the estimated  $CRF_{sc}$  curves, subject 210415 was characterized by a more abrupt increase and faster return to baseline. The RF time-series of these two subjects also exhibited different profiles, while their  $RRF_{sc}$  curves differed significantly from the canonical  $RRF_{stand}$  and the population-specific  $RRF_{ppl}$  curve. The rest of the three scans of subject 210415 exhibited  $RRF_{sc}$  curves similar to the  $RRF_{ppl}$  (Fig. 2d) while the curves found for the rest of the three scans of subject 307127 were similar to the curve derived from the R2a scan shown in Fig. 3 (supplementary Figs. 4-7).

To better understand the properties of the scan-specific  $PRF_{sc}$  curves, we investigated whether the times of positive and negative peak depend on physiological variables (e.g. mean and variance of HR). Among the different combinations that we tested, significant correlations were found only between the shape of the  $CRF_{sc}$  curves and the subjects' HR. Specifically, shorter times for the negative  $CRF_{sc}$  peak correlated with higher mean HR values (Fig. 4a). Furthermore, we examined whether HR and RF fluctuations had a stronger effect on the GS under specific physiological states. Fig. 4b shows that HR values were significantly anticorrelated with the fraction of the GS explained by the cardiac regressor (as quantified by the correlation coefficient between model prediction and GS), whereas RF variance values were found to be significantly correlated to the fraction of the GS explained by the respiratory regressor (Fig. 4c).





### 3.3.1 Effect of sample size and duration of scan on PRF parameter estimation

To assess the effect of the number of subjects on the reliability of the obtained population-specific models, we repeated estimation of the model parameters using 10 different randomized subject cohorts of different sizes (see Methods). In Fig. 6a, it can be seen that the performance of the population-specific models increased monotonically between 1 and 10 subjects and reached a plateau at a mean correlation of around 51% and 53% for the  $PRF_{ppl}$  and  $PRF_{ppl}^{sc}$  models, respectively. We also examined the effect of the scan duration, which may considerably affect model reliability, particularly in the case of  $PRF_{sc}$ . Fig. 6b shows a comparison of the performance achieved for the least ( $PRF_{ppl}$ ) and most ( $PRF_{sc}$ ) flexible models as a function of scan duration. The  $PRF_{ppl}$  model yielded higher correlation values for short scan durations (44% for a one-minute duration), while these values stabilized around 51% for scan durations above 5 minutes. The  $PRF_{sc}$  model yielded poorer performance for scan durations shorter than 5 minutes, and its performance improved for longer scan durations, eventually reaching a mean correlation of 56% (15-minute scan duration). Interestingly, these two models yielded very similar performance for a 5-minute scan duration, which is the minimum scan duration typically used in rs-fMRI studies.

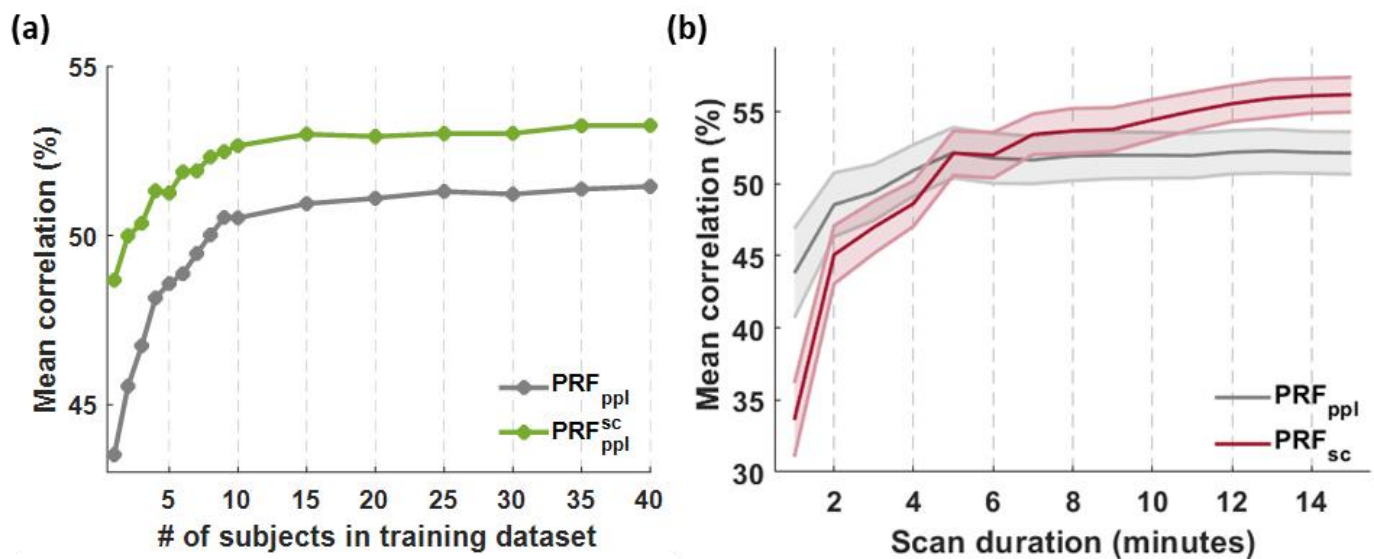


**Fig. 6. Effect of sample size and scan duration on the performance of PRF models.** (a) The PRF parameters in the population-specific models  $PRF_{ppl}$  and  $PRF_{ppl}^{sc}$  were estimated using subsets of subjects and the performance of the models was assessed on the remaining subjects. Both models reached a plateau at a sample size of around 10 subjects (b) The performance of the least flexible model (i.e.  $PRF_{ppl}$ ) and the most flexible model (i.e.  $PRF_{sc}$ ) was assessed on reduced scan durations. Our results suggest that for scan duration longer than 5 minutes the scan-specific  $PRF_{sc}$  model explained more variance in GS than the  $PRF_{ppl}$  model and a more profound difference was observed as the scan duration increased.

### 3.4 Model performance in individual voxels

435 The comparison of the models was repeated on a voxel-wise basis in ROIs. The ROIs were defined for each model separately and included the 5% of voxels in the brain with the highest goodness of fit (see Methods). The analysis at the voxel-level yielded similar findings with the analysis based on the fit to the GS (Fig. 7). The full  $PRF_{sc}$  model (i.e.  $CRF_{sc}$  and  $RRF_{sc}$ ) yielded the best performance among all models with a mean correlation around 24% (note the lower values compared to GS). Importantly, the  $PRF_{sc}^{vxl}$  model demonstrated slightly lower mean correlation compared to the  $PRF_{sc}$  model, even though it allows variability in the estimated curves across voxels. For all the examined models, the respiration-related component exhibited higher mean correlation compared to the cardiac-related component, although the difference was not statistically significant ( $p > 0.05$ ). The analysis for assessing model performance at the voxel level was also performed on resting-state fMRI data that were corrected for physiological noise with FIX. The results were similar to the results derived from the raw data, although the overall mean correlation was decreased in the latter case. The  $PRF_{sc}$  model again illustrated the best performance with a mean correlation of around 17%.

The brain areas affected by fluctuations in HR and breathing pattern were mainly areas in gray matter and close to blood vessels (Fig. 8). Unsurprisingly, the standard methods ( $PRF_{stand}$ ) and the proposed methods yielded similar maps regarding the areas more affected by physiological noise. However, the explained variance obtained using the proposed  $PRF$  curves was significantly higher compared to the standard curves.

450 The statistical maps shown in Fig. 8 demonstrate much finer detail compared to previous related studies (Birn et al., 2008; Chang et al., 2009; Golestani et al., 2015) which is in part due to the higher spatial resolution (2 mm isotropic voxels) fMRI data acquired in the HCP. However, another factor that may have affected the resolution is the spatial smoothing performed during the preprocessing. To better understand its effect, we extracted these maps without spatial smoothing as well as with a spatial filter with a larger FWHM value (6 mm instead of 3 mm). As shown in Supplementary Figs. 8-9, larger FWHM values resulted in higher correlation values. Overall, our results suggest that a FWHM value of 3 mm yields a good compromise between the resulting signal-to-noise (SNR) ratio and the spatial resolution of the regional maps related to physiological effects on fMRI time-series.

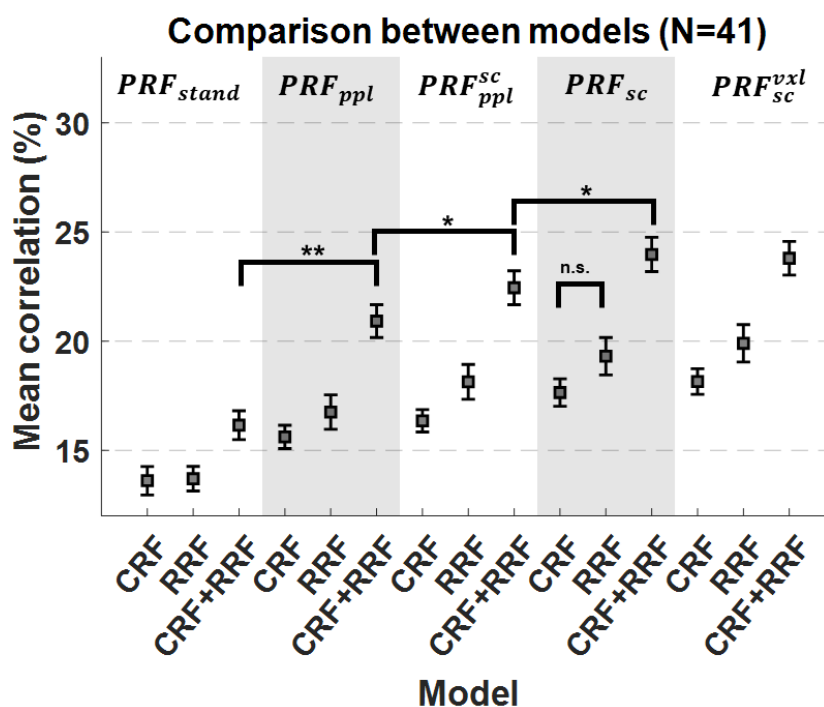
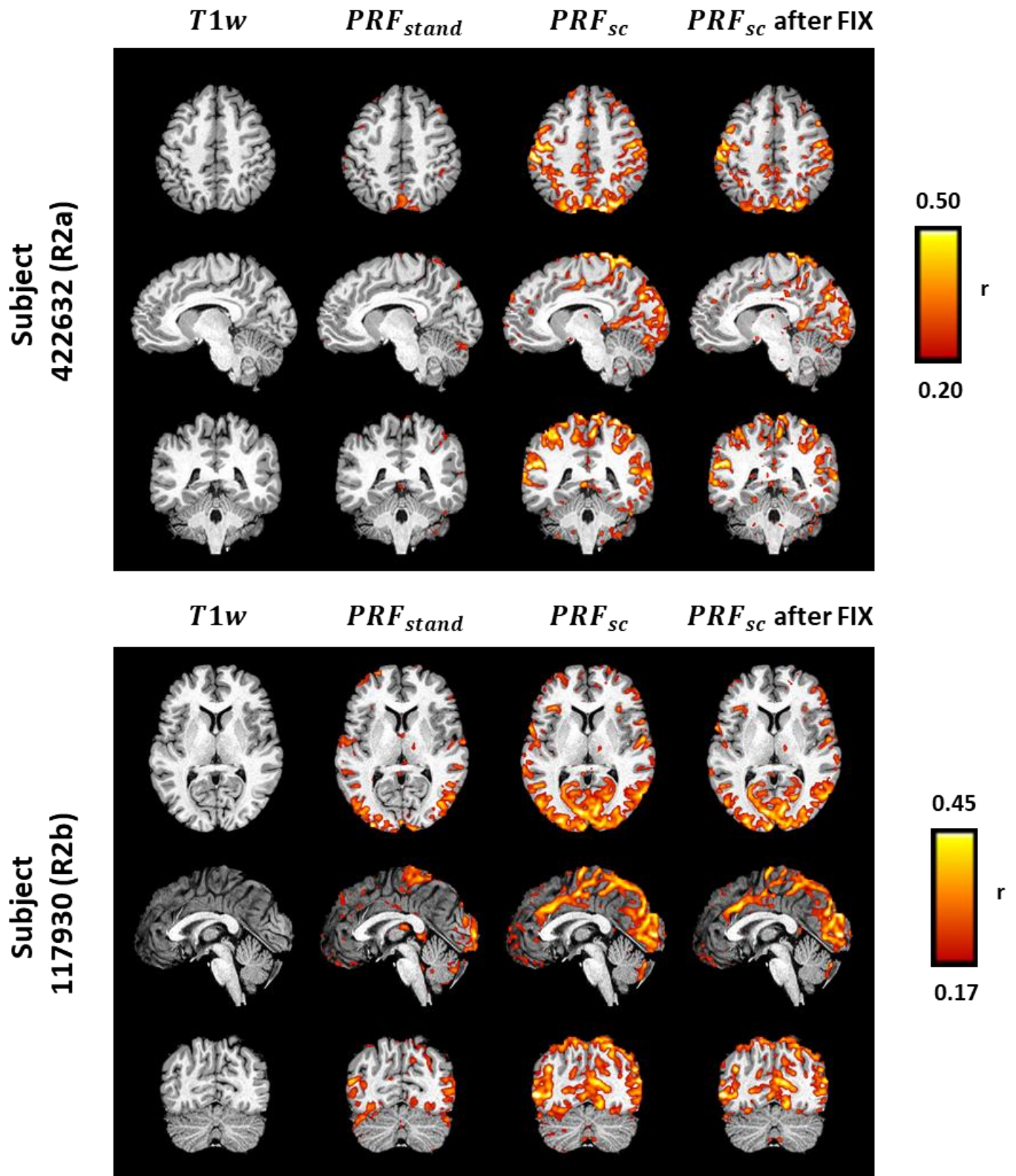
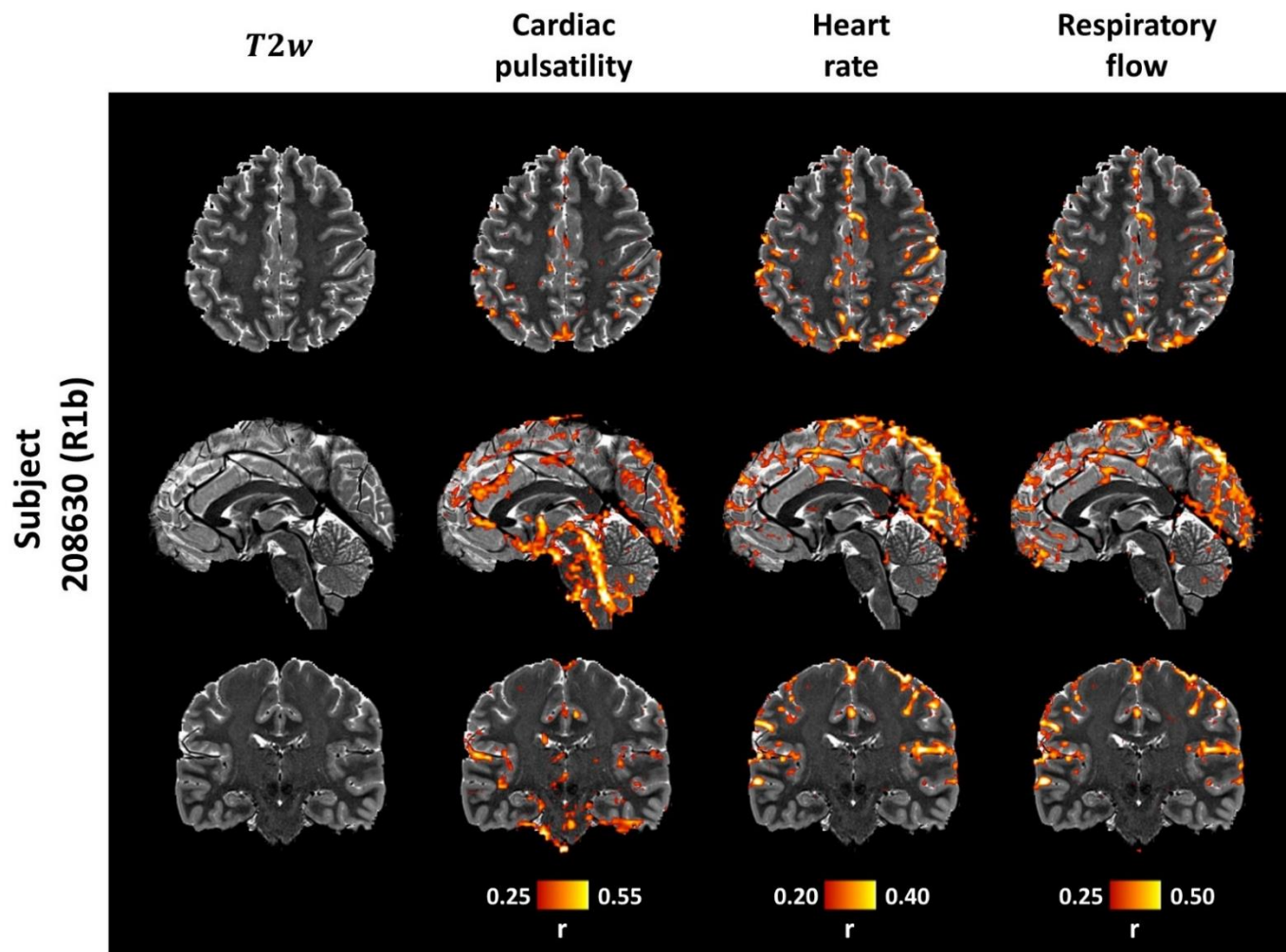


Fig. 7. Correlation values between physiological model predictions and voxel-specific timeseries, averaged over all voxels within the ROI of each model. The squares and error bars indicate the mean and standard error of the means of all subjects. As in the case of GS-based analysis, the population-specific  $PRF_{ppl}$  model yielded significantly increased performance compared to the standard methods ( $PRF_{stand}$ ). Overall, the best performance was achieved with the scan-specific model  $PRF_{sc}$ . \* $p < 10^{-8}$ , \*\* $p < 10^{-13}$ .



**Fig. 8.** Correlation maps between the physiological model predictions and fMRI timeseries for two representative subjects. (1<sup>st</sup> column)  $T_1$ -weighted images; (2<sup>nd</sup> & 3<sup>rd</sup> column) maps derived with the standard ( $PRF_{stand}$ ) and scan-specific ( $PRF_{sc}$ ) model, respectively; (4<sup>th</sup> column) maps derived with the scan-specific model when applied on data previously corrected with FIX. Overall, all models account for substantial variance in gray matter as well as near large vessels.

460 Finally, the contribution of different sources of physiological noise was examined. Specifically, the 6 parameters  
corresponding to the cardiac-related regressors in RETROICOR (3<sup>rd</sup> order), estimated during preprocessing, were used  
to construct the pulsatility-driven component of each voxel timeseries, which was subsequently correlated with each  
voxel timeseries to extract the correlation map related to pulsatility. The maps related to HR and RF were extracted  
separately by employing the scan-specific models ( $CRF_{sc}$  and  $RRF_{sc}$  respectively). Fig. 9 shows the contribution of each  
465 physiological source for a representative subject on  $T_2$ -weighted structural images, instead of the typical  $T_1$ -weighted  
images, as  $T_2$ -weighted images yield better contrast for visualizing vessels. We observe that not all areas with large  
vessels were equally affected by pulsatility or fluctuations in HR and the breathing pattern. Furthermore, changes in HR  
and the breathing pattern mostly affected areas in gray matter in the cerebrum, whereas pulsatility affected areas close to  
the brainstem. Fig. 10 illustrates the spatial patterns averaged across all subjects for the three aforementioned  
physiological noise sources. As in Fig. 9, HR and RF effects were found to be more pronounced in distinct areas as  
470 compared to cardiac pulsatility. We could not examine whether the changes in HR and breathing patterns were more  
pronounced in voxels located around draining veins and sinuses rather than arteries, as the HCP does not include images  
for differentiating veins from arteries. However, a visual comparison with voxel-wise probabilistic maps of veins and  
arteries developed in (Bernier et al., 2018) suggests that voxels nearby large draining vessels may be mostly affected by  
changes in HR and breathing patterns, whereas voxels close to arteries may be mostly affected by cardiac pulsatility.



**Fig. 9.** Contribution of different physiological noise sources in fMRI for a representative subject. (1<sup>st</sup> column)  $T_2$ -weighted images; (2<sup>nd</sup> column) correlation maps related to cardiac pulsatility as modelled with RETROICOR; (3<sup>rd</sup> column) correlation maps related to HR as modelled with the scan-specific model  $CRF_{sc}$ ; (4<sup>th</sup> column) correlation maps related to RF as modelled with the scan-specific model  $RRF_{sc}$ . While the effect of all physiological sources appears mostly in areas close to vessels, cardiac pulsatility effects are more pronounced around the brainstem, whereas HR and RF effects are more prominent in the occipital and parietal lobes.

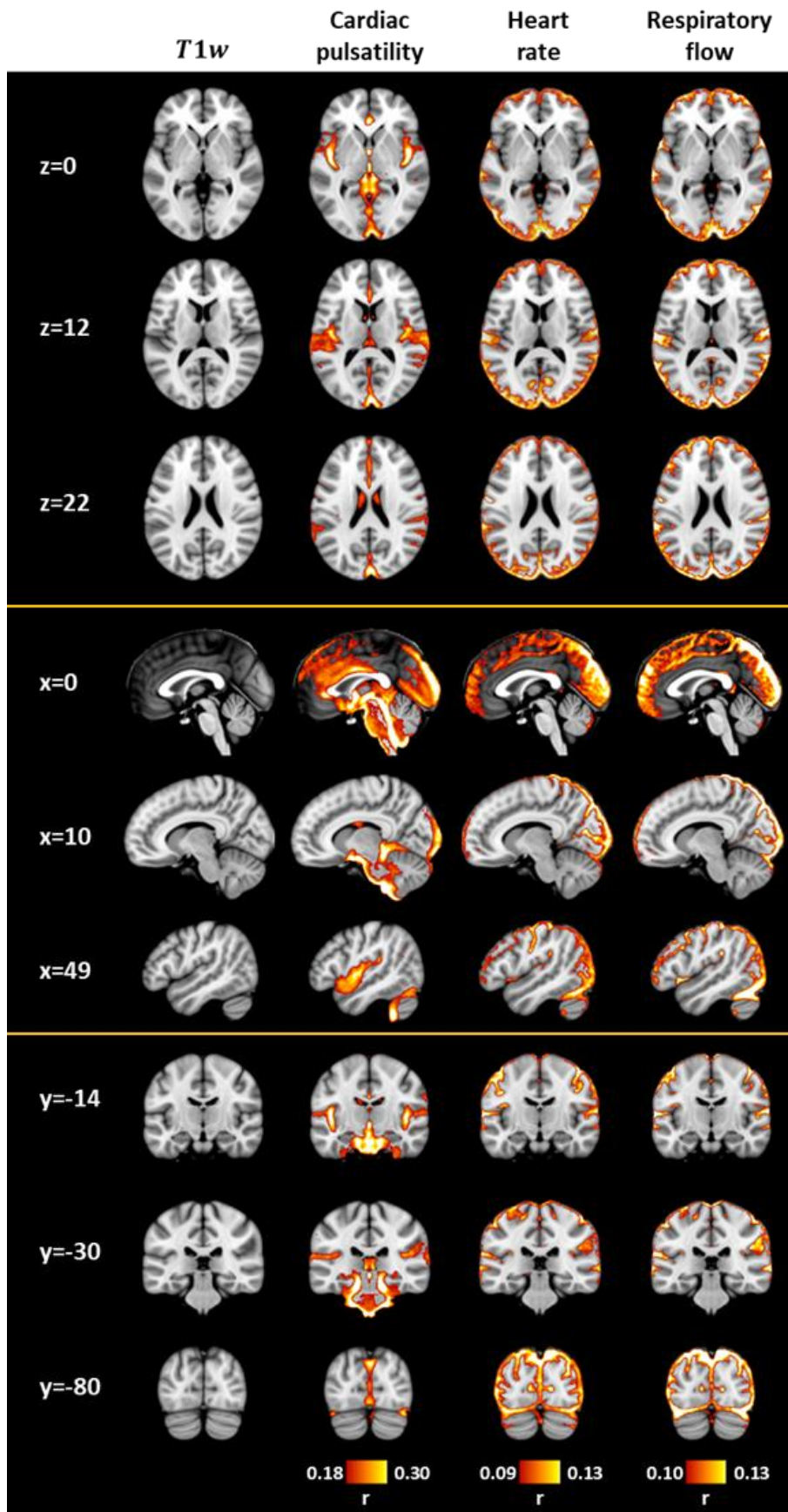


**Fig. 10. Contribution of different physiological noise sources in fMRI averaged across all subjects.** (1<sup>st</sup> column) MNI152 standard-space  $T_1$ -weighted average structural template image (1 mm isometric voxel); (2<sup>nd</sup> column) correlation maps related to cardiac pulsatility as modelled with RETROICOR; (3<sup>rd</sup> column) correlation maps related to HR as modelled with the scan-specific model  $CRF_{sc}$ ; (4<sup>th</sup> column) correlation maps related to RF as modelled with the scan-specific model  $RRF_{sc}$ . BOLD fluctuations due to cardiac pulsatility were more pronounced close to the basilar and vertebral artery, in the 4<sup>th</sup> ventricle, in the superior sagittal sinus, in the lateral sulcus, in the occipital lobe and in the anterior cingulate cortex. On the other hand, BOLD fluctuations due to changes in HR and RF were widespread in gray matter and more pronounced in frontal and posterior brain regions, as well as in sinuses such as the superior sagittal sinus and the transverse sinuses.

## 4. Discussion

We have rigorously examined the effect of the choice of physiological response functions on the investigation of physiological effects (HR and breathing pattern) on fMRI. To do so, we proposed a novel modeling framework to obtain accurate estimates of the  $PRF$  curves. Linear convolution models, whereby physiological variables are convolved with suitable  $PRF$  curves, were employed to model the associated physiological-driven BOLD fluctuations. The  $PRF$  curves were estimated using numerical optimization techniques that present several advantages compared to previously used techniques (Birn et al., 2008; Chang et al., 2009; Falahpour et al., 2013; Golestani et al., 2015). The structure of the curves was defined as the double gamma function which is also the basis of the canonical HRF in SPM and  $RRF_{stand}$  (Birn et al., 2008), and its parameters were restricted within physiologically plausible ranges. The population-specific models  $PRF_{ppl}$  demonstrated significantly better fit on the GS as well as in individual voxel time-series compared to the standard models  $PRF_{stand}$  (Fig. 5, Fig. 7). The scan-specific models  $PRF_{sc}$  outperformed  $PRF_{ppl}$  while no significant differences were found between the scan-specific models  $PRF_{sc}$  and voxel-specific models  $PRF_{sc}^{vxl}$ . The between-scan variability in the  $PRF$  curves was partly attributed to physiological factors such as the subject's mean HR during a scan. Overall, HR was found to explain higher frequency fluctuations on the GS than RF (Fig. 3). Consistent with previous findings, changes in HR and breathing pattern (breathing rate and depth) had a strong effect across widespread regions in the gray matter (Birn et al., 2008; Chang et al., 2009).

### 4.1 Population specific vs standard $PRF$ curves

Using the proposed framework, we derived population specific curves ( $CRF_{ppl}$  and  $RRF_{ppl}$ ), which explained a substantially larger fraction of GS and individual voxel time-series variance compared to the standard models  $PRF_{stand}$  (Fig. 5, Fig. 7). The population-specific HR model  $CRF_{ppl}$  demonstrated considerably faster dynamics than  $CRF_{stand}$  (Chang et al., (2009); Fig. 2a). Some of the main differences in the two studies that may explain the results are the following: a) in Chang et al., (2009) the resting-state scan was performed with eyes closed instead of eyes open as done in the HCP data used here, and b)  $CRF_{stand}$  was obtained by first estimating the  $CRF$  with the method of maximum likelihood in individual voxels and then averaging across voxels and subjects, whereas, in the present study, similar to Falahpour et al. (2013),  $CRF$  estimation was based on the GS of each scan, which is strongly driven by physiological noise, and, thus, yields higher SNR. In addition to these, one of the reasons for the faster dynamics observed in the  $CRF$  curves in the present study is the fact that in previous studies (Chang et al., 2009; Falahpour et al., 2013; Golestani et al., 2015) HR was initially averaged within a time window of 4-6 s and subsequently downsampled to a low TR (e.g. 3 s) before further analysis, disregarding fast fluctuations in HR. Also, due to sinus arrhythmia effects commonly observed in young subjects, the smoothed HR may tend to become more similar to the respiratory cycle. As a result,  $CRF_{stand}$  may capture some of the effects of respiration on the BOLD signal.

Differences, albeit to a smaller extent, were also found between the population-specific curve  $RRF_{ppl}$  and the standard curve  $RRF_{stand}$  (Birn et al., 2008; Fig. 2d). However, in the proposed model, a different feature (RF) was used as an input and, thus, direct comparisons between  $RRF_{ppl}$  and  $RRF_{stand}$  should be made with caution. The RF was introduced here as a physiological variable derived from the respiratory signal and was preferred to RVT (Birn et al., 2008) as it does not require peak detection, a task that is not always straightforward for respiratory signals as the breathing volume and rate during spontaneous breathing can vary over a wide range across time. A possible explanation for the increased performance of the proposed  $RRF_{ppl}$  model compared to the standard method is that  $RRF_{ppl}$  was estimated using resting-state data with the RF and the GS as the input and output of the model, whereas in Birn et al. (2008),  $RRF_{stand}$  was derived from the BOLD response induced by a deep breath without incorporating the RVT in the estimation stage. Note that Birn et al. (2008) also reported a poor fit of their method in resting-state fMRI, which was improved only when allowing time-shifting separately for each voxel, an approach that was followed later by (Bianciardi et al., 2009; Chang and Glover, 2009b). However, time shifting has been shown to inflate the correlation statistics and, therefore, validation of the optimal temporal shift is needed in future studies (Bright et al., 2016).

The population specific curve  $CRF_{ppl}$  (Fig. 2a) was characterized by a peak at 1.2 s and an undershoot at 7.0 s. A possible explanation about the first peak is that increases (decreases) in HR are briefly followed by an increase (decrease) in cardiac output and, in turn, in CBF and BOLD signal. On the other hand, the undershoot may indicate the presence of a negative feedback mechanism (e.g. decrease of stroke volume and, thus, cardiac output or decrease in relative distribution of cardiac output to the cerebral vasculature) which ensures that CBF is maintained at normal levels. A positive peak followed by a negative peak was observed for  $RRF_{ppl}$  as well (Fig. 2d). A possible explanation for this behavior is the following: Increases in RF are followed by increases in the levels of  $O_2$  in cerebral blood which in turn lead to a decrease in levels of deoxygenated blood and an increase in the BOLD signal. However, increases in RF are also followed by decreases in levels of  $CO_2$  in the blood, which is a strong vasodilator. As a result, decreases in levels of  $CO_2$  are followed by a decrease in CBF and BOLD signal. This vasoconstriction, however, is likely a slower process, which can explain the decrease in BOLD signal with a minimum peak at about 13 seconds after the RF increase. In a similar manner, a decrease in RF would lead to an initial decline in BOLD signal followed by a slow overshoot.

## 4.2 Variability in $PRF$ curves across subjects and scans

Among the different physiological models examined in this study, the scan specific model  $PRF_{sc}$  yielded the best performance (Fig. 5, Fig. 7). This suggests that physiological response functions do not only vary across subjects but also across scans of the same subject. Importantly, our results suggest that scan-specific curves can be robustly derived from whole-brain resting-state fMRI data with durations longer than 5 minutes and high sampling rate (e.g.  $TR=0.72$ ) (Fig. 6b). As the physiological origin of the  $CRF$  and  $RRF$  curves is different, their form is discussed separately.

Visual inspection of the scan-specific curves  $CRF_{sc}$  revealed differences across subjects and across sessions within-subjects. A more systematic comparison revealed that the time of the negative peak of the curve was strongly dependent on the mean HR of the subject, with shorter times linked to higher mean HR (Fig. 4a). As the mean HR was found to vary significantly between the two sessions within-subject (Fig. 1), this may explain the differences in  $CRF_{sc}$  curves across sessions. Differences in  $CRF_{sc}$  curves across sessions within-subject could be attributed also to differences in arterial blood pressure that may vary significantly between scans collected at different days. However, we could not examine this factor as blood pressure measurements were not collected at the day of each fMRI scan. The finding that the time of negative peak of the curve was associated with higher mean HR may suggest that when HR is higher, CBF is also higher and a fast negative feedback is more critical to prevent extreme values of CBF.

In our work, we assumed that the relationship between HR and the BOLD signal can be described with a linear time-invariant system. However, it may be the case that a time-varying system, the parameters of which are expressed as a function of the time-varying mean (or instantaneous) HR and possibly blood pressure may explain the fluctuations in GS more accurately. Moreover, we observed that  $CRF_{sc}$  explained a larger fraction of GS variance for scans with a low mean HR. Subsequent analysis showed a strong positive correlation between the mean HR and fluctuations in HR (results not shown here), which could indicate that a time-varying  $CRF$  is more appropriate for cases where HR is high and varies significantly. On the other hand, a possible explanation that scans with high mean HR yielded a weaker correlation between fluctuations in HR and GS is that in these scans the subjects were more stressed, which explains the high mean HR, and tended to move more distorting the fMRI data, including the GS, or that the subjects were in a state of higher arousal levels and, consequently a significant component of the GS fluctuations was neuronal-driven.

The population specific curve  $RRF_{ppl}$  demonstrated relatively mild differences compared to the  $RRF_{stand}$ . On the other hand, the scan specific curves  $RRF_{sc}$  exhibited a larger degree of variability across subjects and scans compared to  $CRF_{sc}$ , with curves for a large number of scans having only negative values, instead of the commonly observed positive peak followed by an undershoot (Birn et al., 2008; Chang et al., 2009; Power et al., 2017). These differences could not be attributed to the different individual patterns in BR or RF. Nonetheless, the proportion of GS variance explained with RF was found to be correlated with RF variance (Fig. 4c). RF was defined as the squared derivative of the respiratory signal, which has a similar form with the framewise displacement measures proposed in the literature for head motion (Power et al., 2012; van Dijk et al., 2012). Head motion is a main source of noise in fMRI, as it can cause spin history related

575 motion artifacts in the BOLD signal with finite time memory (Friston et al., 1996). In this context, RF could be viewed as an index of relative head motion induced by respiration that is sampled at a higher sampling rate compared to the motion parameters estimated in fMRI preprocessing during volume realignment. As a result, apart from fluctuations due to changes in CO<sub>2</sub> levels, RF, through convolution with the  $RRF_{sc}$ , can potentially remove residuals of motion artifacts that cannot be removed completely with the motion parameters or RETROICOR regressors through linear regression. Moreover, the respiratory-related motion artifacts may be related to the body type and breathing behavior of each subject, as well as the position the subject inside the MRI tube, which could explain the variability of the  $RRF_{sc}$  curves across subjects and sessions within-subject and the improved performance of the scan-specific model compared to a the population-specific model  $RRF_{ppt}$ , particularly in scans with high RF variance.

### 580 4.3 Physiological noise correction with FIX and GSR

585 FIX is a widely-used tool for denoising fMRI data, as it removes fluctuations due to motion and cardiac pulsatility in an automated manner without the need for physiological recordings (Salimi-Khorshidi et al., 2014). HCP has been using it to provide FIX-denoised data and many researchers have been analyzing these data without any further preprocessing (Bijsterbosch et al., 2017; Vidaurre et al., 2017). However, Burgess et al. (2016) have recently demonstrated, using grayordinate plots, that while FIX-denoising substantially reduces spatially specific artifacts, it yields only a mild decrease in global fluctuations.

590 Our study provides further evidence that FIX does not completely remove global artifacts, and particularly fluctuations due to changes in HR and breathing pattern. The effects of these fluctuations are typically widespread within the gray matter and mainly in frontal and posterior brain regions (Fig. 10). As a side note, our analysis showed that cardiac pulsatility that is often modelled with RETROICOR is efficiently removed with FIX (results not shown here). It is well established that spontaneous fluctuations in physiological processes lead to global fluctuations in the fMRI BOLD signal (Chang et al., 2009). Furthermore, these fluctuations may also have a significant effect in rs-FC analyses, including dynamic rs-connectivity (Birn, 2012; Murphy et al., 2013; Nikolaou et al., 2016) and, therefore, should be taken into consideration in the analysis. However, it has been suggested that spatial ICA, which is used in FIX as well as in other ICA-based denoising techniques such as ICA-AROMA (Pruim et al., 2015) is mathematically, by design, unable to separate global temporal artifacts from fMRI data (Glasser et al., 2018).

600 The GS, which is simply the BOLD timeseries averaged across all voxels in the brain, is often regressed out from the fMRI data, in conjunction with other nuisance regressors (Aguirre et al., 1997; Fox et al., 2005) or FIX (Burgess et al., 2016; Siegel et al., 2017), in order to correct for global artifacts. GSR has been shown to improve the correspondence of properties of fMRI rs-FC with observations from neuroanatomy (Fox et al., 2009) and to substantially reduce motion-group differences (Burgess et al., 2016). However, there is no consensus yet in the field whether GSR should be performed (Liu et al., 2017; Murphy and Fox, 2017). Murphy et al. (2009) was the first study to mathematically demonstrate that GSR introduces spurious anticorrelations in rs-FC. Moreover, many recent studies have reported strong correlations between the fluctuations or amplitude of GS and neuronal-related measures such as electrophysiological activity from intracranial recordings (Scholvinck et al., 2010) and vigilance levels (Chang et al., 2016; Falahpour et al., 2018; Wong et al., 2016, 2013). As a result, to facilitate interpretation, reviewers have been recommending the repetition of rs-FC studies with and without GSR to address whether the results can be attributed to GSR or not, while a recent study has developed a measure termed Impact of the Global Average on Functional Connectivity (IGAFC), which quantifies the extent of the impact of GSR on inferences based on seed-based statistical correlation maps (Carbonell et al., 2014). Furthermore, researchers have proposed alternatives to GSR. For example, Glasser et al. (2018) have recently proposed the use of temporal ICA after FIX denoising to preserve the neuronal-related component of the global signal, while removing global structured noise. However, this technique is only applicable to large datasets such as HCP. In addition, Carbonell et al. (2011) have proposed a method based on PCA for regressing out global artifacts and fluctuations that are uncorrelated to network-specific activity, even though it cannot ensure the preservation of global neurophysiological activity.



Our results suggest that a good alternative to GSR are the *PRF* models proposed here. As the physiological regressors are extracted from concurrent physiological recordings, in contrast to GSR and other data-driven techniques, they can account for physiological-driven fluctuations without any possible loss of neuronal-related fluctuations. These models can be trained on a scan-by-scan basis based on the GS and physiological recordings of cardiac activity and respiration. Following the training, the physiological regressors are extracted and can be subsequently removed from the data through linear regression or added in the general linear model as regressors along with other regressors of interest. The codes for the *PRF* models presented here as well as the group-level correlation maps related to cardiac pulsatility, HR and RF (Fig. 10) are publicly available and can be found on <https://github.com/mkassinopoulos/>.

## 5. Conclusion

In this study, we have developed a novel method for removing the effect of fluctuations in HR and breathing patterns in BOLD fMRI data by combining optimization and basis expansion techniques for the robust estimation of subject and scan-specific *PRF<sub>sc</sub>* curves. Our approach was validated on data from the Human Connectome Project (HCP) and achieved improved performance compared to current methods, including the standard *CRF<sub>stand</sub>* and *RRF<sub>stand</sub>*, and FIX.

The proposed framework is of great interest for researchers interested in studying rs-FC in groups where breathing, heart rhythms or cerebrovascular reactivity can differ. Ultimately, better understanding and quantifying physiological effects on fMRI studies can pave the way for understanding the normal and pathological brain as well as accelerate the discovery of connectivity-based biomarkers for diagnosing neurological disorders, as it will contribute towards disentangling the neural vs. physiological sources of rs-FC.

## Acknowledgments

This work was supported by the Natural Sciences and Engineering Research Council of Canada (Discovery Grant 34362 awarded to GDM), the Fonds de la Recherche en Santé - Nature et Technologies (FRQNT; Team Grant PR191780-2016 awarded to GDM) and the Canada First Research Excellence Fund (awarded to McGill University for the Healthy Brains for Healthy Lives initiative). MK acknowledges funding from Québec Bio-imaging Network (QBIN). Data were provided by the Human Connectome Project, WU-Minn Consortium (Principal Investigators: David Van Essen and Kamil Ugurbil; 1U54MH091657) funded by the 16 NIH Institutes and Centers that support the NIH Blueprint for Neuroscience Research; and by the McDonnell Center for Systems Neuroscience at Washington University.

## References

- Aguirre, G.K., Zarahn, E., D'Esposito, M., 1997. Empirical Analyses of BOLD fMRI Statistics. *Neuroimage* 5, 199–212. <https://doi.org/10.1006/nimg.1997.0264>
- Bernier, M., Cunnane, S.C., Whittingstall, K., 2018. The morphology of the human cerebrovascular system. *Hum. Brain Mapp.* 4962–4975. <https://doi.org/10.1002/hbm.24337>
- Bianciardi, M., Fukunaga, M., van Gelderen, P., Horovitz, S.G., de Zwart, J.A., Shmueli, K., Duyn, J.H., 2009. Sources of functional magnetic resonance imaging signal fluctuations in the human brain at rest: a 7 T study. *Magn. Reson. Imaging* 27, 1019–1029. <https://doi.org/10.1016/j.mri.2009.02.004>
- Bijsterbosch, J., Harrison, S., Duff, E., Alfaro-Almagro, F., Woolrich, M., Smith, S., 2017. Investigations into within- and between-subject resting-state amplitude variations. *Neuroimage* 159, 57–69. <https://doi.org/10.1016/j.neuroimage.2017.07.014>
- Birn, R.M., 2012. The role of physiological noise in resting-state functional connectivity. *Neuroimage* 62, 864–870.

<https://doi.org/10.1016/j.neuroimage.2012.01.016>

660 Birn, R.M., Diamond, J.B., Smith, M.A., Bandettini, P.A., 2006. Separating respiratory-variation-related fluctuations from neuronal-activity-related fluctuations in fMRI. *Neuroimage* 31, 1536–48. <https://doi.org/10.1016/j.neuroimage.2006.02.048>

Birn, R.M., Smith, M. a., Jones, T.B., Bandettini, P. a., 2008. The respiration response function: The temporal dynamics of fMRI signal fluctuations related to changes in respiration. *Neuroimage* 40, 644–654. <https://doi.org/10.1016/j.neuroimage.2007.11.059>

665 Biswal, B., Yetkin, F.Z., Haughton, V.M., Hyde, J.S., 1995. Functional connectivity in the motor cortex of resting human brain using echo-planar MRI. *Magn. Reson. Med.* 34, 537–541. <https://doi.org/10.1002/mrm.1910340409>

Bright, M.G., Murphy, K., 2015. Is fMRI “noise” really noise? Resting state nuisance regressors remove variance with network structure. *Neuroimage* 114, 158–169. <https://doi.org/10.1016/j.neuroimage.2015.03.070>

Bright, M.G., Tench, C.R., Murphy, K., 2016. Potential pitfalls when denoising resting state fMRI data using nuisance regression. *Neuroimage* 1–10. <https://doi.org/10.1016/j.neuroimage.2016.12.027>

670 Burgess, G.C., Kandala, S., Nolan, D., Laumann, T.O., Power, J.D., Adeyemo, B., Harms, M.P., Petersen, S.E., Barch, D.M., 2016. Evaluation of Denoising Strategies to Address Motion-Related Artifacts in Resting-State Functional Magnetic Resonance Imaging Data from the Human Connectome Project. *Brain Connect.* 6, 669–680. <https://doi.org/10.1089/brain.2016.0435>

675 Caballero-Gaudes, C., Reynolds, R.C., 2017. Methods for cleaning the BOLD fMRI signal. *Neuroimage* 154, 128–149. <https://doi.org/10.1016/j.neuroimage.2016.12.018>

Carbonell, F., Bellec, P., Shmuel, A., 2014. Quantification of the impact of a confounding variable on functional connectivity confirms anti-correlated networks in the resting-state. *Neuroimage* 86, 343–353. <https://doi.org/10.1016/j.neuroimage.2013.10.013>

680 Carbonell, F., Bellec, P., Shmuel, A., 2011. Global and System-Specific Resting-State fMRI Fluctuations Are Uncorrelated: Principal Component Analysis Reveals Anti-Correlated Networks. *Brain Connect.* 1, 496–510. <https://doi.org/10.1089/brain.2011.0065>

Chang, C., Cunningham, J.P., Glover, G.H., 2009. Influence of heart rate on the BOLD signal: The cardiac response function. *Neuroimage* 44, 857–869. <https://doi.org/10.1016/j.neuroimage.2008.09.029>

685 Chang, C., Glover, G.H., 2009a. Effects of model-based physiological noise correction on default mode network anti-correlations and correlations. *Neuroimage* 47, 1448–1459. <https://doi.org/10.1016/j.neuroimage.2009.05.012>

Chang, C., Glover, G.H., 2009b. Relationship between respiration, end-tidal CO<sub>2</sub>, and BOLD signals in resting-state fMRI. *Neuroimage* 47, 1381–1393. <https://doi.org/10.1016/j.neuroimage.2009.04.048>

690 Chang, C., Leopold, D.A., Schölvinck, M.L., Mandelkow, H., Picchioni, D., Liu, X., Ye, F.Q., Turchi, J.N., Duyn, J.H., 2016. Tracking brain arousal fluctuations with fMRI. *Proc. Natl. Acad. Sci.* 113, 4518–4523. <https://doi.org/10.1073/pnas.1520613113>

Churchill, N.W., Strother, S.C., 2013. PHYCAA+: An optimized, adaptive procedure for measuring and controlling physiological noise in BOLD fMRI. *Neuroimage* 82, 306–325. <https://doi.org/10.1016/j.neuroimage.2013.05.102>

Dagli, M.S., Ingelholm, J.E., Haxby, J. V., 1999. Localization of cardiac-induced signal change in fMRI. *Neuroimage* 9, 407–415. <https://doi.org/10.1006/nimg.1998.0424>

695 Demirtaş, M., Tornador, C., Falcón, C., López-Solà, M., Hernández-Ribas, R., Pujol, J., Menchón, J.M., Ritter, P., Cardoner, N., Soriano-Mas, C., Deco, G., 2016. Dynamic functional connectivity reveals altered variability in functional connectivity among patients with major depressive disorder. *Hum. Brain Mapp.* 00. <https://doi.org/10.1002/hbm.23215>

- 700 Falahpour, M., Chang, C., Wong, C.W., Liu, T.T., 2018. Template-based prediction of vigilance fluctuations in resting-state fMRI. *Neuroimage* 174, 317–327. <https://doi.org/10.1016/j.neuroimage.2018.03.012>
- Falahpour, M., Refai, H., Bodurka, J., 2013. Subject specific BOLD fMRI respiratory and cardiac response functions obtained from global signal. *Neuroimage* 72, 252–264. <https://doi.org/10.1016/j.neuroimage.2013.01.050>
- 705 Fox, M.D., Snyder, A.Z., Vincent, J.L., Corbetta, M., Van Essen, D.C., Raichle, M.E., 2005. The human brain is intrinsically organized into dynamic, anticorrelated functional networks. *Proc. Natl. Acad. Sci. U. S. A.* 102, 9673–8. <https://doi.org/10.1073/pnas.0504136102>
- Fox, M.D., Zhang, D., Snyder, A.Z., Raichle, M.E., 2009. The global signal and observed anticorrelated resting state brain networks. *J. Neurophysiol.* 101, 3270–83. <https://doi.org/10.1152/jn.90777.2008>
- Friston, K.J., Williams, S., Howard, R., Frackowiak, R.S., Turner, R., 1996. Movement-related effects in fMRI time-series. *Magn. Reson. Med.* 35, 346–355. [https://doi.org/DOI 10.1002/mrm.1910350312](https://doi.org/DOI%2010.1002/mrm.1910350312)
- 710 Glasser, M.F., Coalson, T.S., Bijsterbosch, J.D., Harrison, S.J., Harms, M.P., Anticevic, A., Van Essen, D.C., Smith, S.M., 2018. Using temporal ICA to selectively remove global noise while preserving global signal in functional MRI data. *Neuroimage* 181, 692–717. <https://doi.org/10.1016/j.neuroimage.2018.04.076>
- 715 Glasser, M.F., Smith, S.M., Marcus, D.S., Andersson, J.L.R., Auerbach, E.J., Behrens, T.E.J., Coalson, T.S., Harms, M.P., Jenkinson, M., Moeller, S., Robinson, E.C., Sotiropoulos, S.N., Xu, J., Yacoub, E., Ugurbil, K., Van Essen, D.C., 2016. The Human Connectome Project’s neuroimaging approach. *Nat. Neurosci.* 19, 1175–87. <https://doi.org/10.1038/nn.4361>
- Glasser, M.F., Sotiropoulos, S.N., Wilson, J.A., Coalson, T.S., Fischl, B., Andersson, J.L., Xu, J., Jbabdi, S., Webster, M., Polimeni, J.R., Van Essen, D.C., Jenkinson, M., 2013. The minimal preprocessing pipelines for the Human Connectome Project. *Neuroimage* 80, 105–124. <https://doi.org/10.1016/j.neuroimage.2013.04.127>
- 720 Glover, G.H., Li, T.Q., Ress, D., 2000. Image-based method for retrospective correction of physiological motion effects in fMRI: RETROICOR. *Magn. Reson. Med.* 44, 162–167. [https://doi.org/10.1002/1522-2594\(200007\)44:1<162::AID-MRM23>3.0.CO;2-E](https://doi.org/10.1002/1522-2594(200007)44:1<162::AID-MRM23>3.0.CO;2-E)
- Golestani, A.M., Chang, C., Kwinta, J.B., Khatamian, Y.B., Jean Chen, J., 2015. Mapping the end-tidal CO<sub>2</sub> response function in the resting-state BOLD fMRI signal: Spatial specificity, test-retest reliability and effect of fMRI sampling rate. *Neuroimage* 104, 266–277. <https://doi.org/10.1016/j.neuroimage.2014.10.031>
- 725 Greicius, M.D., Krasnow, B., Reiss, A.L., Menon, V., 2003. Functional connectivity in the resting brain: a network analysis of the default mode hypothesis. *Proc Natl Acad Sci U S A* 100, 253–258. <https://doi.org/10.1073/pnas.0135058100> [pii]
- Holland, J.H., 1975. *Adaptation in Natural and Artificial Systems*. University of Michigan Press, Ann Arbor, MI.
- 730 Hu, X., Le, T.H., Parrish, T., Erhard, P., 1995. Retrospective estimation and correction of physiological fluctuation in functional MRI. *Magn. Reson. Med.* 34, 201–212. <https://doi.org/10.1002/mrm.1910340211>
- Jenkinson, M., Beckmann, C.F., Behrens, T.E.J., Woolrich, M.W., Smith, S.M., 2012. FSL. *Neuroimage* 62, 782–90. <https://doi.org/10.1016/j.neuroimage.2011.09.015>
- 735 Jenkinson, M., Smith, S., 2001. A global optimisation method for robust affine registration of brain images. *Med. Image Anal.* 5, 143–156. [https://doi.org/10.1016/S1361-8415\(01\)00036-6](https://doi.org/10.1016/S1361-8415(01)00036-6)
- Jones, T.B., Bandettini, P.A., Birn, R.M., 2008. Integration of motion correction and physiological noise regression in fMRI. *Neuroimage* 42, 582–590. <https://doi.org/10.1016/j.neuroimage.2008.05.019>
- 740 Kasper, L., Bollmann, S., Diaconescu, A.O., Hutton, C., Heinzle, J., Iglesias, S., Hauser, T.U., Sebold, M., Manjaly, Z.M., Pruessmann, K.P., Stephan, K.E., 2017. The PhysIO Toolbox for Modeling Physiological Noise in fMRI Data. *J. Neurosci. Methods* 276, 56–72. <https://doi.org/10.1016/j.jneumeth.2016.10.019>

Kay, K.N., Rokem, A., Winawer, J., Dougherty, R.F., Wandell, B.A., 2013. GLMdenoise: A fast, automated technique for denoising task-based fMRI data. *Front. Neurosci.* 7, 1–15. <https://doi.org/10.3389/fnins.2013.00247>

Leonardi, N., Richiardi, J., Ville, D. Van De, 2013. Functional Connectivity Eigennetworks Reveal Different Brain Dynamics in Multiple Sclerosis Patients. *IEEE Int. Symp. Biomed. Imaging* 524–527.

745 Liang, X., Connelly, A., Calamante, F., 2015. Voxel-wise functional connectomics using arterial spin labeling fMRI: the role of denoising. *Brain Connect.* 5, 150528105119009. <https://doi.org/10.1089/brain.2014.0290>

Liu, T.T., Nalci, A., Falahpour, M., 2017. The global signal in fMRI: Nuisance or Information? *Neuroimage* 150, 213–229. <https://doi.org/10.1016/j.neuroimage.2017.02.036>

750 Murphy, K., Birn, R.M., Bandettini, P.A., 2013. Resting-state fMRI confounds and cleanup. *Neuroimage* 80, 349–359. <https://doi.org/10.1016/j.neuroimage.2013.04.001>

Murphy, K., Birn, R.M., Handwerker, D.A., Jones, T.B., Bandettini, P.A., 2009. The impact of global signal regression on resting state correlations: Are anti-correlated networks introduced? *Neuroimage* 44, 893–905. <https://doi.org/10.1016/j.neuroimage.2008.09.036>

755 Murphy, K., Fox, M.D., 2017. Towards a consensus regarding global signal regression for resting state functional connectivity MRI. *Neuroimage* 154, 169–173. <https://doi.org/10.1016/j.neuroimage.2016.11.052>

Napadow, V., Dhond, R., Conti, G., Makris, N., Brown, E.N., Barbieri, R., 2008. Brain correlates of autonomic modulation: Combining heart rate variability with fMRI. *Neuroimage* 42, 169–177. <https://doi.org/10.1016/j.neuroimage.2008.04.238>

760 Nikolaou, F., Orphanidou, C., Papakyriakou, P., Murphy, K., Wise, R.G., Mitsis, G.D., 2016. Spontaneous physiological variability modulates dynamic functional connectivity in resting-state functional magnetic resonance imaging. *Philos. Trans. A. Math. Phys. Eng. Sci.* 374, 20150183-. <https://doi.org/10.1098/rsta.2015.0183>

Ogawa, S., Lee, T., 1990. Brain magnetic resonance imaging with contrast dependent on blood oxygenation. *Proc. ...* 87, 9868–72. <https://doi.org/10.1073/pnas.87.24.9868>

765 Patel, N., Padhiyar, N., 2015. Modified genetic algorithm using Box Complex method: Application to optimal control problems. *J. Process Control* 26, 35–50. <https://doi.org/10.1016/j.jprocont.2015.01.001>

Power, J.D., Barnes, K.A., Snyder, A.Z., Schlaggar, B.L., Petersen, S.E., 2012. Spurious but systematic correlations in functional connectivity MRI networks arise from subject motion. *Neuroimage* 59, 2142–2154. <https://doi.org/10.1016/j.neuroimage.2011.10.018>

770 Power, J.D., Plitt, M., Laumann, T.O., Martin, A., 2017. Sources and implications of whole-brain fMRI signals in humans. *Neuroimage* 146, 609–625. <https://doi.org/10.1016/j.neuroimage.2016.09.038>

Pruim, R.H.R., Mennes, M., van Rooij, D., Llera, A., Buitelaar, J.K., Beckmann, C.F., 2015. ICA-AROMA: A robust ICA-based strategy for removing motion artifacts from fMRI data. *Neuroimage* 112, 267–277. <https://doi.org/10.1016/j.neuroimage.2015.02.064>

775 Qing, Z., Dong, Z., Li, S., Zang, Y., Liu, D., 2015. Global signal regression has complex effects on regional homogeneity of resting state fMRI signal. *Magn. Reson. Imaging* 33, 1306–1313. <https://doi.org/10.1016/j.mri.2015.07.011>

Salimi-Khorshidi, G., Douaud, G., Beckmann, C.F., Glasser, M.F., Griffanti, L., Smith, S.M., 2014. Automatic denoising of functional MRI data: Combining independent component analysis and hierarchical fusion of classifiers. *Neuroimage* 90, 449–468. <https://doi.org/10.1016/j.neuroimage.2013.11.046>

780 Scholvinck, M.L., Maier, A., Ye, F.Q., Duyn, J.H., Leopold, D.A., 2010. Neural basis of global resting-state fMRI activity. *Proc. Natl. Acad. Sci.* 107, 10238–10243. <https://doi.org/10.1073/pnas.0913110107>

Sheline, Y.I., Price, J.L., Yan, Z., Mintun, M.A., 2010. Resting-state functional MRI in depression unmasks increased connectivity between networks via the dorsal nexus. *Proc. Natl. Acad. Sci.* 107, 11020–11025.

<https://doi.org/10.1073/pnas.1000446107>

- 785 Shmueli, K., van Gelderen, P., de Zwart, J. a., Horovitz, S.G., Fukunaga, M., Jansma, J.M., Duyn, J.H., 2007. Low-frequency fluctuations in the cardiac rate as a source of variance in the resting-state fMRI BOLD signal. *Neuroimage* 38, 306–320. <https://doi.org/10.1016/j.neuroimage.2007.07.037>
- Siegel, J.S., Mitra, A., Laumann, T.O., Seitzman, B.A., Raichle, M., Corbetta, M., Snyder, A.Z., 2017. Data quality influences observed links between functional connectivity and behavior. *Cereb. Cortex* 27, 4492–4502. <https://doi.org/10.1093/cercor/bhw253>
- 790 Smith, S.M., Fox, P.T., Miller, K.L., Glahn, D.C., Fox, P.M., Mackay, C.E., Filippini, N., Watkins, K.E., Toro, R., Laird, A.R., Beckmann, C.F., 2009. Correspondence of the brain’s functional architecture during activation and rest. *Proc. Natl. Acad. Sci. U. S. A.* 106, 13040–5. <https://doi.org/10.1073/pnas.0905267106>
- van den Heuvel, M.P., Hulshoff Pol, H.E., 2010. Exploring the brain network: A review on resting-state fMRI functional connectivity. *Eur. Neuropsychopharmacol.* 20, 519–534. <https://doi.org/10.1016/j.euroneuro.2010.03.008>
- 795 van Dijk, K.R.A., Sabuncu, M.R., Buckner, R.L., 2012. The influence of head motion on intrinsic functional connectivity MRI. *Neuroimage* 59, 431–438. <https://doi.org/10.1016/j.neuroimage.2011.07.044>
- Van Essen, D.C., Smith, S.M., Barch, D.M., Behrens, T.E.J., Yacoub, E., Ugurbil, K., 2013. The WU-Minn Human Connectome Project: An overview. *Neuroimage* 80, 62–79. <https://doi.org/10.1016/j.neuroimage.2013.05.041>
- 800 Vidaurre, D., Smith, S.M., Woolrich, M.W., 2017. Brain network dynamics are hierarchically organized in time. *Proc. Natl. Acad. Sci.* 201705120. <https://doi.org/10.1073/pnas.1705120114>
- Wise, R.G., Ide, K., Poulin, M.J., Tracey, I., 2004. Resting fluctuations in arterial carbon dioxide induce significant low frequency variations in BOLD signal. *Neuroimage* 21, 1652–1664. <https://doi.org/10.1016/j.neuroimage.2003.11.025>
- 805 Wong, C.W., DeYoung, P.N., Liu, T.T., 2016. Differences in the resting-state fMRI global signal amplitude between the eyes open and eyes closed states are related to changes in EEG vigilance. *Neuroimage* 124, 24–31. <https://doi.org/10.1016/j.neuroimage.2015.08.053>
- Wong, C.W., Olafsson, V., Tal, O., Liu, T.T., 2013. The amplitude of the resting-state fMRI global signal is related to EEG vigilance measures. *Neuroimage* 83, 983–990. <https://doi.org/10.1016/j.neuroimage.2013.07.057>
- 810 Woodward, N.D., Cascio, C.J., 2015. Resting-State Functional Connectivity in Psychiatric Disorders. *JAMA psychiatry* 72, 743–744. <https://doi.org/10.1001/jamapsychiatry.2015.0101.2>